



Geochemical and Isotopic Signature of Pyrite as a Proxy for Fluid Source and Evolution in the Candelaria-Punta del Cobre Iron Oxide Copper-Gold District, Chile

I. del Real,^{1,1,*} J.F.H. Thompson,¹ A. C. Simon,² and M. Reich^{3,4}

¹*Department of Earth and Atmospheric Sciences, Cornell University, Snee Hall, Ithaca, New York 14850*

²*Department of Earth and Environmental Sciences, University of Michigan, Ann Arbor, Michigan 48109*

³*Department of Geology and Andean Geothermal Center of Excellence (CEGA), Facultad de Ciencias Físicas y Matemáticas (FCFM), Universidad de Chile, Plaza Ercilla 803, Santiago 8320000, Chile*

⁴*Millennium Nucleus for Metal Tracing Along Subduction, Facultad de Ciencias Físicas y Matemáticas (FCFM), Universidad de Chile, Santiago 8320000, Chile*

Abstract

Pyrite is ubiquitous in the world-class iron oxide copper-gold (IOCG) deposits of the Candelaria-Punta del Cobre district, documented from early to late stages of mineralization and observed in deep and shallow levels of mineralized bodies. Despite its abundance, the chemical and isotopic signature of pyrite from the Candelaria-Punta del Cobre district, and most IOCG deposits worldwide, remains poorly understood. We evaluated in situ chemical and isotopic variations at the grain scale in a set of pyrite-bearing samples collected throughout the district in order to characterize and further understand the nature of mineralization in this IOCG system. Our multianalytical approach integrated synchrotron micro-X-ray fluorescence (μ -XRF) mapping of pyrite grains with electron probe microanalysis and laser ablation-inductively coupled plasma-mass spectrometry data, and sulfur isotope determinations using secondary ion mass spectrometry (SIMS) complemented with bulk sulfur isotope analyses of coeval pyrite, chalcopyrite, and anhydrite. Synchrotron μ -XRF elemental concentration maps of individual pyrite grains reveal a strong zonation of Co, Ni, As, and Se. The observed relationships between Ni and Se are interpreted to reflect changes in temperature and redox conditions during ore formation and provide constraints on fluid evolution. Co and Ni concentrations and ratios suggest contributions from magmas of mafic-intermediate composition. Pyrite chemical concentrations reflect potential stratigraphic controls, where the sample from the upper part of the stratigraphy diverges from trends formed by the rest of the sample set from lower stratigraphic levels. The SIMS $\delta^{34}\text{S}$ values of pyrite (and chalcopyrite) range between -2 up to 10‰ , and bulk $\delta^{34}\text{S}$ values of pyrite range between 4 up to 12‰ . The majority of the $\delta^{34}\text{S}$ analyses, falling between -1 and 2‰ , indicate a magmatic source for sulfur and, by inference, for the hydrothermal ore fluid(s). Variation in the $\delta^{34}\text{S}$ signature can be explained by changes in the redox conditions, fluid sources, and/or the temperature of the hydrothermal fluid. The Se/S ratio combined with $\delta^{34}\text{S}$ values in pyrite is consistent with mixing between a magmatic-hydrothermal fluid and a fluid with a probable basinal signature. The results of this study are consistent with the hydrothermal fluids responsible for mineralization in the Candelaria-Punta del Cobre district being predominantly of magmatic origin, plausibly from mafic-intermediate magmas based on the Ni-Co content in pyrite. External fluid incursion, potentially from a basinal sedimentary source, occurred late in the evolution of the system, adding additional reduced sulfur as pyrite. There is no evidence to suggest that the late fluid added significant Cu-Au mineralization, but this cannot be ruled out. Finally, the data reveal that trace element ratios coupled with spatially resolved sulfur isotope data in pyrite are powerful proxies to track the magmatic-hydrothermal evolution of IOCG systems and help constrain the source of their contained metals.

Introduction

The source of hydrothermal fluids in iron oxide copper-gold (IOCG) deposits has been a controversial topic for several decades, since the discovery in the 1970s of the giant Precambrian Olympic Dam deposit in Australia (Roberts and Hudson, 1983; Hitzman et al., 1992). Multiple interpretations and models have been proposed to explain the formation of these deposits involving different fluids, including oxidized saline brines derived from evaporites (Barton and Johnson, 1996; Hitzman, 2000), magmatic fluids derived from major intrusions (Marschik and Fontboté, 2001b; Pollard, 2006), and combinations of both magmatic and basinal fluids (Williams

et al., 2005; Chiaradia et al., 2006). A connection to Kiruna-type iron oxide-apatite (IOA) deposits has also been proposed (Sillitoe, 2003; Knipping et al., 2015a; Reich et al., 2016; Barra et al., 2017; Simon et al., 2018), with Fe-rich and S-poor IOA mineralization representing the deeper roots of some Andean IOCG systems.

IOCG deposits are complex, relatively rare, and overall less studied than well-understood systems such as porphyry copper deposits. The complexity in IOCG deposits may reflect diverse tectonic settings, a range of host-rock and structural environments, and the involvement of more than one hydrothermal fluid. The lack or scarce amount of quartz in IOCG deposits hinders the use of fluid inclusions for determining temperature, fluid composition and salinity, and the potential source of hydrothermal fluids (Groves et al., 2010). Even though alteration paragenesis has been well defined in some areas (e.g., the Great Bear district; Corriveau et al., 2016), it

¹Corresponding author: e-mail, idelreal@gmail.com

*Present address: Millennium Nucleus for Metal Tracing Along Subduction, Facultad de Ciencias Físicas y Matemáticas (FCFM), Universidad de Chile, Santiago 8320000, Chile.

can vary from deposit to deposit, with the presence of iron oxides and Cu-rich sulfides being the only common features in all IOCG deposits (Hitzman, 2000). The use of mineral chemistry and isotopic systems provides alternative approaches for assessing the nature of the hydrothermal fluid and characterizing IOCG deposits (e.g., De Haller et al., 2006; Rusk et al., 2010; Reich et al., 2016, among others)

Most IOCG deposits contain pyrite (FeS_2), ranging from an accessory phase in pyrite-poor systems ($\sim <1\%$; e.g., Salobo, Brazil, and Olympic Dam, Australia; Haynes et al., 1995; Requia and Fontboté, 1999) to major amounts in pyrite-rich systems ($\sim >1\%$; e.g., Ernest Henry, Australia, and Candelaria, Chile; Marschik and Fontboté, 2001b; Williams et al., 2005; Rusk et al., 2010). The presence of pyrite in most IOCG deposits provides an opportunity to compare their character and composition and potentially to use the resulting data to constrain hydrothermal fluid sources and evolution. Pyrite has been successfully used as a proxy for characterizing hydrothermal fluids in a large variety of mineral deposits, including Carlin-type gold, volcanogenic massive sulfide (VMS), sedimentary-hosted Cu/U, Archean to Mesozoic lode, and epithermal gold deposits, among others (Cook and Chryssoulis, 1990; Hannington et al., 1999; Reich et al., 2005; Barker et al., 2009; Cook et al., 2009; Large et al., 2009; Peterson and Mavrogenes, 2014; Gregory et al., 2015; Keith et al., 2016; Tanner et al., 2016; Román et al., 2019). Pyrite chemistry has been used as a record of fluid evolution in porphyry copper systems (Reich et al., 2013), and, in some cases, it has provided evidence for the transition from porphyry to epithermal environments (Franchini et al., 2015). Pyrite chemistry has also been used in the Los Colorados IOA deposit (Chile) to suggest a link with IOCG deposits (Reich et al., 2016). Finally, pyrite chemistry has been evaluated to constrain the source of hydrothermal fluids in three IOCG deposits: Sossego, Brazil (Monteiro et al., 2008), Ernest Henry, Australia (Rusk et al., 2010), and more recently, the Marcona IOA and Mina Justa IOCG deposits in Peru (Li et al., 2018).

In addition to using the chemical composition of pyrite to constrain hydrothermal processes, the sulfur isotope composition ($\delta^{34}\text{S}$) of pyrite can constrain the fluid source and, by inference, metal sources and ore-forming processes (Ohmoto, 1972; Rye and Ohmoto, 1974; Ohmoto and Goldhaber, 1997). This tool has been used on pyrite separates from IOCG deposits where variable $\delta^{34}\text{S}$ indicates a complex fluid source history (Marschik and Fontboté, 2001b; Benavides et al., 2007; De Haller and Fontboté, 2009; Rusk et al., 2010; Zhao and Zhou, 2011). In situ sulfur isotope analyses using secondary ion mass spectrometry (SIMS) has been used to measure changes in the isotopic signature ($\delta^{34}\text{S}$) within single pyrite grains in IOCG deposits (Li et al., 2018), with the results revealing isotopic variations at the grain scale. Comparisons between sulfur isotope signatures and pyrite chemistry from IOCG deposits has produced mixed results varying from no clear correlation with inferred mineralizing processes (e.g., Ernest Henry; Rusk et al., 2010) to potential evidence for least two different fluid sources (e.g., Mina Justa; Li et al., 2018).

In this contribution we present a new and comprehensive data set on pyrite chemistry from the Candelaria-Punta del Cobre district using three different microanalytical approaches: electron probe microanalysis (EPMA), laser

ablation-inductively coupled plasma-mass spectroscopy (LA-ICP-MS), and synchrotron micro-X-ray fluorescence (synchrotron μ -XRF). EPMA and LA-ICP-MS data were used to evaluate varying concentrations of trace elements in pyrite grains. Synchrotron μ -XRF was used for creating element concentration imagery maps of the pyrite grains used for this study. LA-ICP-MS data were integrated with in situ sulfur isotope analyses ($\delta^{34}\text{S}$) of pyrite and coexisting chalcopyrite using SIMS. Bulk sulfur isotope data of pyrite and anhydrite determined by isotope ratio mass spectrometry (IRMS) were used to constrain temperature variations of the hydrothermal fluid. We relate the chemical zonation of trace elements in pyrite with changes in the depth of formation, based on stratigraphic relationships and the mineral paragenesis in the district. We also correlate chemical variation in pyrite with variations of sulfur isotopes within the same pyrite grains. Our extensive data set provides constraints on fluid evolution, sources, temperature, and redox conditions at the Candelaria-Punta del Cobre district with implications for the origin of the district and IOCG systems.

Geologic Background

IOCG deposits in north-central Chile form part of the Andean IOA-IOCG belt, which extends from immediately north of Santiago to north of Antofagasta with the majority of the deposits located between Tal Tal and Vallenar (Fig. 1). The belt continues north from the southern border of Peru to Lima for a total length in the Andes of $\sim 2,000$ km. Deposit ages range from ~ 90 to ~ 165 Ma, with El Espino being the youngest at 88.4 ± 1.2 Ma (Lopez et al., 2014; del Real and Arriagada, 2015) and Montecristo and Julia the oldest at 164 ± 11 and 159 ± 3 Ma (Boric et al., 1990; Espinoza et al., 1996). Within the belt, Mantoverde, Raúl Condestable, Mina Justa, and Candelaria are major copper deposits, with Candelaria being the most significant producer. Candelaria came into production in 1995 and current (September 2019) open-pit proven and probable reserves are 459 million tonnes (Mt) at 0.5% Cu (www.lundin.com). If all the mines and past producers in the Candelaria-Punta del Cobre district are considered, the total endowment is approximately 13 Mt of contained Cu (del Real et al., 2018).

IOCG deposits in northern Chile are commonly spatially associated with, or hosted in, faults that form part of the Atacama fault system (Fig. 1; Arabasz, 1971; Grocott et al., 1994; Espinoza et al., 1996; Grocott and Taylor, 2002). As with IOCG deposits worldwide, more than one model has been proposed for the formation of Andean IOCG deposits based on the interpretation of data from several different systems. Models have invoked different fluid sources: (1) oxidized saline brines derived from evaporites that formed in continental back-arc basins during the Upper Jurassic and Lower Cretaceous (Barton and Johnson, 1996; Hitzman, 2000) and (2) magmatic-hydrothermal fluids that evolved from temporally and spatially associated igneous intrusions (Marschik and Fontboté, 2001b; Sillitoe, 2003; Pollard, 2006; del Real et al., 2018). Both transtensional (Arévalo et al., 2006; Groves et al., 2010; Lopez et al., 2014; Richards et al., 2017) and transpressional (Chen et al., 2013; del Real et al., 2018) tectonic settings have been proposed coincident with the formation of IOCG deposits in the Andean belt.

The Candelaria-Punta del Cobre district includes 10 different active mines: Candelaria, Candelaria Norte, Alcaparrosa, Santos, Atacama Kozan, Granate, Punta del Cobre, Mantos

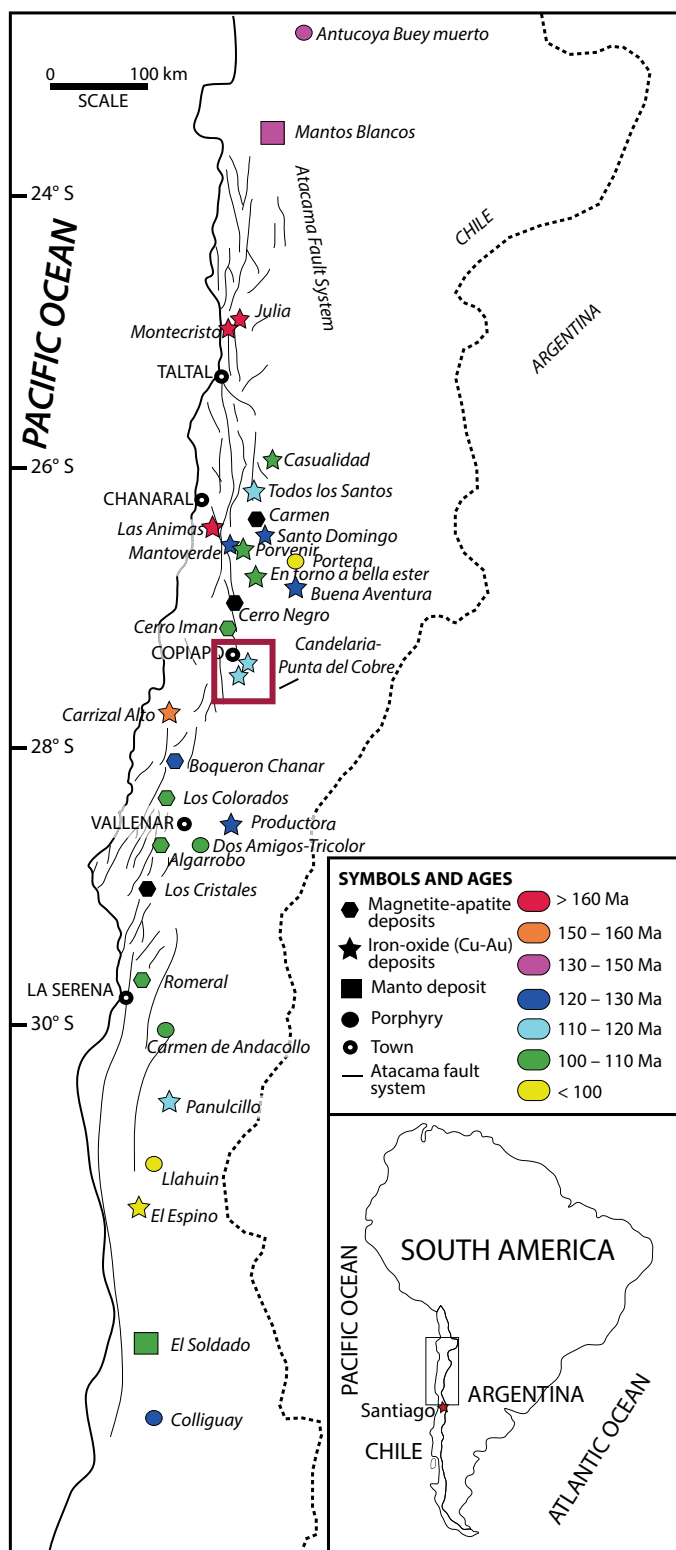


Fig. 1. Location of IOCG, IOA, manto-type, and porphyry deposits formed during the Upper Jurassic-Lower Cretaceous in northern Chile (from del Real et al., 2018). Inset shows location of study area in South America.

del Cobre, Carola, and Las Pintadas (Fig. 2A). The main mineralizing event occurred at ~115 Ma (Mathur et al., 2002; del Real et al., 2018) coeval with the emplacement of the Copiapó batholith just west of the main deposits (Marschik and Söllner, 2006; Fig. 2A). Mineralization is mostly hosted in the Punta del Cobre Formation, which is divided into four main units: the lower andesite unit, the dacite unit, volcanic-sedimentary unit, and the upper andesite unit (Fig. 2A, B; Marschik and Fontboté, 2001a; del Real et al., 2018). Several small mineralized bodies are hosted in the overlying marine sedimentary Abundancia Formation (e.g., Las Pintadas), which formed within the Chañarcillo basin. There is no evidence that the exposed parts of the Copiapó batholith generated ore fluids (del Real et al., 2018), but minor vein-hosted mineralization is found in the batholith.

The majority of the IOCG mineralization in the district is hosted in the upper part of the lower andesite unit and the overlying volcanic-sedimentary and dacite units, all within the Punta del Cobre Formation. Mineralization is hosted in fault zones, breccias, and specific lithologies. North-northwest faults are the dominant host for vertically extensive orebodies. Fault-hosted orebodies are the dominant style of mineralization in the eastern part of the district located along the east side of the Copiapó Valley. Stratigraphically controlled mineralization forms extensive stratabound orebodies (“mantos”), which are most abundant in the western part of the district where the most important lithological host, the volcano-sedimentary sequence, is best developed (del Real et al., 2018). Textural evidence suggests that the hydrothermal system evolved and advanced upward over time (del Real et al., 2018). The earliest event was dominated by magnetite-actinolite in stratigraphically controlled mantos and extensive zones of disseminated magnetite-actinolite in the deeper parts of the Candelaria system. Magnetite-actinolite was subsequently overprinted by chalcopyrite-pyrite-dominant mineralization in veins, fractures, and disseminated replacement with associated magnetite-actinolite-biotite-K-feldspar alteration (Marschik and Fontboté, 2001b; del Real et al., 2018). In addition to magnetite, iron oxides include widespread secondary magnetite (in the form of mushketovite) and hematite in the upper part of some deposits.

Sampling and Analytical Methods

Thirteen pyrite-bearing representative samples from the Candelaria-Punta del Cobre district were selected for this study. The nine samples used for element mapping and in situ sulfur isotope analyses were collected from Santos (samples DH996-2, DH996-21, and DH996-23), Alcaparrosa (samples AD0093-14, AD006-26), Candelaria (samples LD1493-9, ES032-5, and ES032-15), and Las Pintadas (sample LP-1). The four remaining samples, which contain pyrite or chalcopyrite in textural equilibrium with anhydrite (samples AD357-3, AD357-8, AD357-20, and AD009-14), are from the Alcaparrosa deposit. These were selected for whole-grain sulfur isotope analysis coupled with whole-grain pyrite chemistry. The full sample suite represents different ore stages and stratigraphic horizons:

1. Group 1: Samples DH996-21, DH996-23, ES032-15, and AD006-26 are from the main stage of mineralization, the

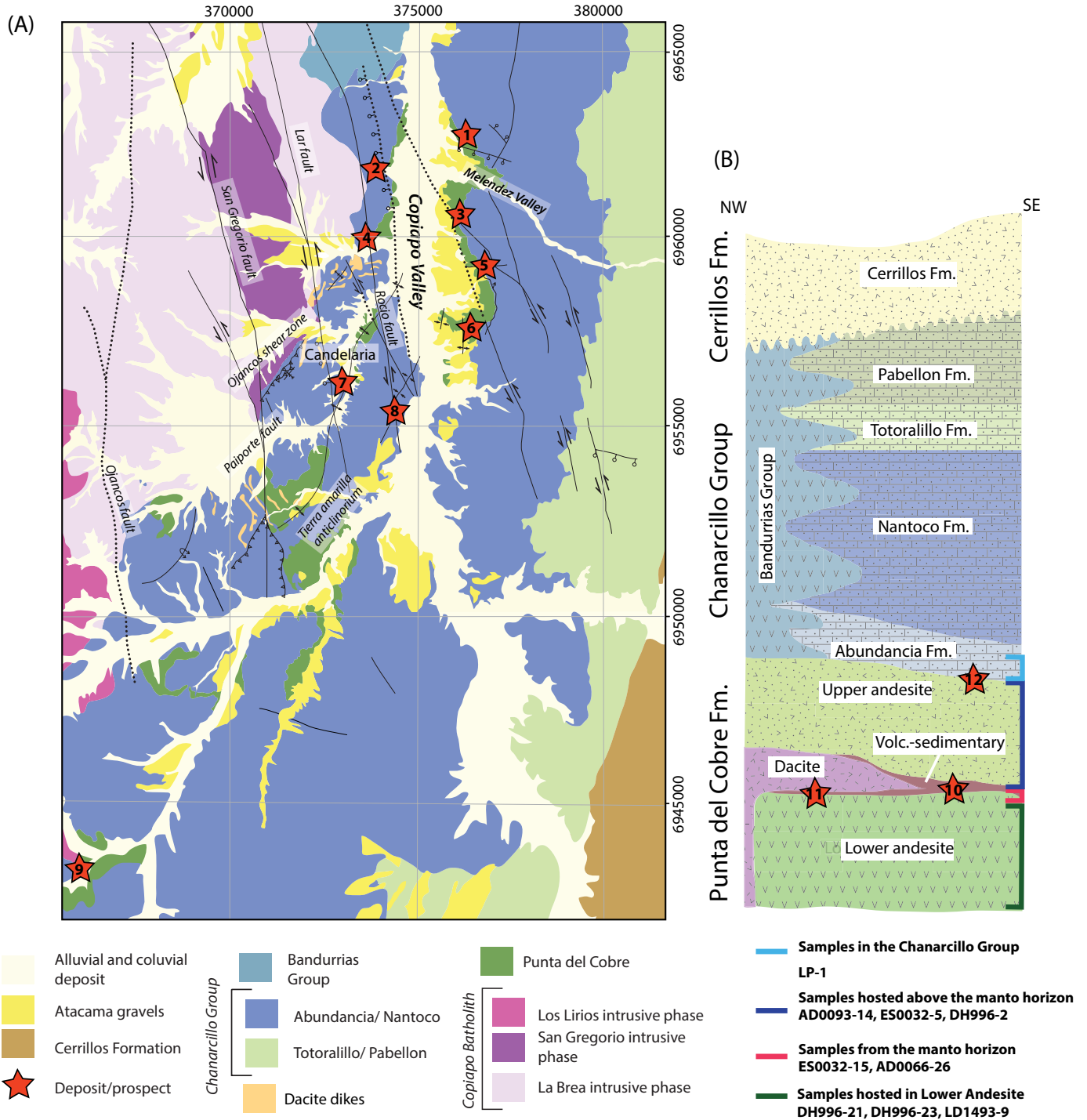


Fig. 2. (A) Simplified geologic map of the Candelaria-Punta del Cobre district with the main IOCG deposits (modified from Arevalo, 1999). UTM coordinates are in datum PSAD56. Stars: 1 = Mantos de Cobre, 2 = Alcaparrosa, 3 = Santos, 4 = Granate, 5 = Punta del Cobre, 6 = Carola, 7 = Candelaria, 8 = Atacama Kozan, 9 = Las Pintadas. (B) Stratigraphic column of the geology in the Candelaria-Punta del Cobre district and the stratigraphic horizons sampled for this work. Stars represent stratigraphic position of deposits used in this study: 10 = Candelaria, Alcaparrosa, 11 = Santos, 12 = Las Pintadas.

first two from structurally controlled orebodies and the other two from manto-style replacement mineralization. Samples from structurally controlled mineralization are located within the lower andesite (Fig. 2B) near its contact

with the dacite unit (~<50–80 m) in the Santos deposit. Samples from manto mineralization are from the volcanic-sedimentary unit (Fig. 2B) in the Candelaria deposit, stratigraphically above the lower andesite.

2. Group 2: Samples DH996-2, ES032-5, and AD0093-14 were collected from mineralized areas peripheral to the main economic mineralization. DH996-2 is from a thin layer in the volcanic-sedimentary unit overlaying dacite (Fig. 2B) ~100 m above the main orebody in the Santos deposit. ES032-5 is from garnet-diopside-actinolite-altered upper andesite (Fig. 2B) ~200 m above the manto horizon just south of the Candelaria deposit. AD0093-14 is from the dacite unit in the Alcaparrosa deposit, ~50 m above the main mineralized orebody.
3. Group 3: Samples LD1493-9, AD0357-3, AD0357-8, AD0357-10, and AD009-14 are from late veins that cut the main manto mineralization. LD1493-9 is located within the lower andesite (Fig. 2B) just below the contact with the volcanic-sedimentary unit in the Candelaria deposit. Samples AD0357-8, AD0357-100 and AD009-14 are from the lower andesite below the main mineralized zone in the Alcaparrosa deposit and sample AD0357-3 is from the dacite unit above this mineralized zone. The latter four samples all contain anhydrite intergrown with pyrite or chalcopyrite.
4. Group 4: Sample LP-1 is from the main ore zone in the Las Pintadas deposit, which is located stratigraphically in the Abundancia Formation (Fig. 2B), the highest stratigraphic level for significant mineralization in the district.

Pyrite grains and aggregates from each sample were examined using polarized-light microscopy at Cornell University supported by backscattered electron (BSE) imaging through the EPMA at Syracuse University (EPMA analytical conditions explained in the next section). Exact locations and more detailed descriptions of the alteration and mineralization for each sample are reported in Table 1. Selected samples were cut and mounted in 25-mm-diameter epoxy mounts and polished down to 60-nm roughness using colloidal silica at the rock preparation laboratory at Syracuse University. The same epoxy mounts were used for most of the analyses performed for this study (synchrotron μ -XRF, EPMA, LA-ICP-MS, and SIMS).

Synchrotron μ -XRF

Synchrotron μ -XRF mapping was performed using beamline F3 at the Cornell High Energy Synchrotron Source (CHESS). Station F3, fed by a bending magnet and a double-multilayer monochromator, provided 14.5-keV incident X-ray energy for these scans. A four-element silicon detector (Vortex ME4) with a Quantum Xpress3 digital signal was employed to collect the XRF signal. Under typical scan conditions of 20- μ m steps and 500-ms dwell time per pixel, typical signals reached >250 kcps per channel with dead time <10%. A well-characterized, natural pyrite sample from the Los Colorados IOA deposit in northern Chile was used as an independent reference for quantifying synchrotron μ -XRF measurements (del Real et al., 2019), since there is currently no commercial pyrite standard available. The scale factor ("monitor efficiency") was adjusted to yield concentrations that matched the reference. The same scale factor was then applied to the subsequently collected pyrite data sets in order to quantify concentrations. Final quantification and correction of the data required application of a variety of statistical methods as previously reported

in del Real et al. (2019). XRF maps were processed using the open-source Praxes software package developed at CHESS (Dale, 2015). Praxes employs PyMCA libraries, developed at the European Synchrotron Research Facilities (ESRF) and is widely used for XRF data processing, spectra fitting, and quantitative analysis (Solé et al., 2007). XRF is a full-spectral technique, meaning that the signal is collected simultaneously for all elements that fluoresce under the experimental conditions. The synchrotron μ -XRF has detection limits near the parts per billion level for most elements, while having no problems in analyzing elements with major element concentrations (e.g., Fe in pyrite). Detection limits calculated using the in-house reference were <1 ppm, with the exception of Co (~6 ppm).

EPMA

Point data was acquired on transects across pyrite grains in order to assess element variation in heterogeneous and zoned crystals. Samples were carbon coated before being analyzed to avoid charge buildup. Transects of 10 to 15 analytical points across grains were completed for each sample. Major and minor element compositional analyses were performed at Syracuse University using a Cameca SXfive field-emission electron microprobe with a LaB6 electron gun and five wavelength dispersive spectrometers. For quantitative measurements, the five wavelength dispersive spectrometers were tuned, and elements were standardized using S and Fe on marcasite, Sb on antimony, Co on cobalt, Ni on nickel silicide, Cu on copper, Zn on sphalerite, As on gallium arsenide, Se on selenium, V on vanadium, and Ag on silver. The beam current was adjusted to ~12,000 counts per second for analyte and X-rays on gas-flow proportional counters. All imaging and quantitative measurements were performed using 15-kV accelerating voltage. Measurements of unknowns were performed using a 20-nA beam current and a 2- μ m beam diameter. Elements were acquired using the following analyzing crystals: LIF for Fe $K\alpha$, Co $K\alpha$, Ni $K\alpha$, Zn $K\alpha$, and Cu $K\alpha$; TAP for As $K\alpha$, and Se $K\alpha$. Counting time was 100 s for Ni $K\alpha$, As $L\alpha$, Se $L\alpha$, Co $K\alpha$, Cu $K\alpha$, and Zn $K\alpha$, and 20 s (10 s in two spectrometers) for Fe $K\alpha$. Background times were determined by peak time divided by two. Because two backgrounds were measured (one on either side of the peak), the total background time measured equals the peak time.

LA-ICP-MS

Similar to EPMA, point data were acquired on transects across pyrite grains in order to assess heterogeneous and zoned grains. Transects were designed to follow those analyzed by EPMA. LA-ICP-MS analyses were carried out at the Queen's University Facility for Isotope Research (QFIR) using a XSeries 2 ICP-MS coupled to a New Wave/ESI Excimer 193-nm laser ablation system. The LA-ICP-MS calibration was initiated by analyzing a U.S. Geological Survey (USGS) glass standard (GSD) to optimize He and Ar flow through the ablation cell and the plasma torch. Optimum plasma conditions were ensured by monitoring uranium oxides (<0.6% UO/U). Point data were obtained using a beam diameter and spot measurement of 75 μ m at a repetition rate of 10 Hz, with a gas blank of 10 to 20 s. The laser beam was focused onto the surface of the sample, and the ICP-MS determined the trace

Table 1. Pyrite Sample Descriptions, Including Paragenesis, Host Rock, and Location of Each Sample Used for this Study

Sample	Lithology	Sample classification	Sulfur isotope analysis	Pyrite type	Description	Depth in drill hole (m)	Location collar (Datum PSAD56)			Trend (°)	Plunge (°)
							North	East	Z surface (m)		
ES032-15	Volcanic-sedimentary unit	Group 1, hosted in mantle stratigraphic horizon	In situ	Single grains	Layers of chalcopyrite-pyrite-pyrrhotite-magnetite-actinolite-feldspar intercalated with layers of biotite-feldspar; pyrrhotite is the main sulfide in the sample; sample paragenetically corresponds to the mantle orebody in the Candelaria deposit	899.8	6958496	373144	707	64	69
AD006-26	Volcanic-sedimentary unit	Group 1, hosted in mantle stratigraphic horizon	In situ	Single grains	Pervasive actinolite-magnetite alteration with patches of epidote and chlorite; minor disseminated feldspar; disseminated chalcopyrite-pyrrhotite-pyrite; sample paragenetically corresponds to the mantle horizon in the Aleparosa deposit	343.55	6962264	374337	484	90	112
DH996-21	Lower andesite	Group 1, hosted in structurally controlled orebody	In situ	Aggregate	Vein of magnetite-pyrite-chalcopyrite with feldspar on the rim and chlorite-sericite patches in the center; chalcopyrite occurs in between pyrite grains or inside them as inclusions; surrounding host rock is obliterated to fine-grained biotite and magnetite; sample corresponds to the main mineralization orebody in the Santos deposit, hosted under the Dacite dome	254.6	696117	376306	503	245.4	106
DH996-23	Lower andesite	Group 1, hosted in structurally controlled orebody	In situ	Single grains	Sample obliterated to fine-grained magnetite-biotite (altered to chlorite)-feldspar-actinolite with patches of epidote; chalcopyrite and pyrite disseminated throughout the sample; sample corresponds to the main mineralization orebody in the Santos deposit, hosted under the Dacite dome	305.6	6961117	376306	503	245.4	106
DH996-2	Volcanic-sedimentary unit	Group 2	In situ	Single grains	Sample altered to fine-grained feldspar-biotite (replaced to chlorite and sericite) with minor disseminated chlorite and magnetite and epidote patches; chalcopyrite, pyrite, and magnetite disseminated throughout the sample; sample corresponds to shallow minor mineralization hosted on top of the Dacite dome in the Santos deposit	13.5	6961117	376306	503	245.4	106
ES032-5	Upper andesite	Group 2	In situ	Aggregate	Upper andesite intercalated sediments obliterated to garnet, diopside, and scapolite; patches of calcite and actinolite-plagioclase; plagioclase is altered to sericite; between the garnets there is pyrite with minor magnetite and chalcopyrite; sample corresponds to minor mineralization hosted on top of the Candelaria deposit	455	6958496	373144	707	64	69

Table 1. (Cont.)

Sample	Lithology	Sample classification	Sulfur isotope analysis	Pyrite type	Description	Depth in drill hole (m)	Location collar (Datum PSAD56)			Trend (°)	Plunge (°)
							North	East	Z surface (m)		
AD0093-14	Dacite dome	Group 2	In situ	Single grains	Disseminated magnetite-feldspar with minor patches of actinolite and biotite and calcite; patches of magnetite-chalcopyrite-pyrite-biotite; sample corresponds to minor disseminated mineralization within the Aleparrosa deposit	185.7	6962294	374337	484	90	115
LD1493-9	Lower andesite	Group 3	In situ	Single grains	Chalcopyrite-pyrite-actinolite with minor feldspar and magnetite vein; surrounding host rock is obliterated to actinolite and magnetite with minor epidote and chlorite disseminated; sample corresponds to a late vein that cuts through the main mineralization and alteration in the Candelaria deposit	138.3	6956239	373365	544	245	99
AD0357-10	Lower andesite	Group 3	Bulk	NA	Anhydrite-pyrite-chalcopyrite vein and minor chlorite in the edges; sample corresponds to late vein that cuts the main alteration in the Lower Andesite	97.25	6962301	373935	471	90	1.5
AD0357-8	Lower andesite	Group 3	Bulk	NA	Anhydrite-chalcopyrite vein; sample corresponds to late vein that cuts the main alteration in the Lower Andesite, which is autobrecciated	79.65	6962301	373935	471	90	1.5
AD0357-3	Dacite dome	Group 3	Bulk	NA	Anhydrite-pyrite-chalcopyrite and minor chlorite-epidote in the edges; sample corresponds to late vein that cuts the main alteration in dacite dome	25.65	6962301	373935	471	90	1.5
AD009-14	Lower andesite	Group 3	Bulk	NA	Anhydrite-pyrite vein; sample corresponds to late vein that cuts the main alteration in the Lower Andesite	190.15	6961426	373935	493	0	0
LP-1	Abundancia Formation	Group 4	In situ	Single grains	Sample is heavily altered to biotite (partially altered to chlorite), fine-grained feldspar, minor epidote, and actinolite; disseminated chalcopyrite with minor pyrite and magnetite	1.004	6947654	367142	1,004	Outcrop	

element concentrations in the ablated material. Analyses were bracketed by calibrations using USGS glass standards (GSC-1G, GSD-1G, and GSE-1G), and external standards (BHVO-1, MASS-1, and NIST612) were used to monitor instrument drift and correct for elemental bias and laser yield. Raw data were plotted against the element calibration curves created using USGS glass standards to quantify the ablated areas. Each spot measurement was monitored as it was acquired through a live cam in order to take note of any inclusions that were ablated during the analysis. Data were collected in time-resolved graphics mode to monitor possible compositional heterogeneities that might be present in the sample at the scale of the laser sampling and to monitor the interelemental fractionation that can occur during laser ablation analysis. The software package PlasmaLab was used for selecting and monitoring the data integration space of each point and element analyzed.

In situ sulfur isotope analysis

In situ sulfur isotope measurements of pyrite and coeval chalcopyrite reported in this study were conducted using the WiseSIMS CAMECA IMS 1280 large radius multicollector ion microprobe in the Department of Geoscience of the University of Wisconsin, Madison. Analytical procedures were similar to those previously reported for sulfur two-isotope (^{32}S and ^{34}S) analyses (Kozdon et al., 2010). Sulfide mounts in epoxy resin were Au coated (~ 30 nm). The secondary $^{32}\text{S}^-$, $^{32}\text{S}^1\text{H}^-$, and $^{34}\text{S}^-$ ions were simultaneously collected by three Faraday cup detectors. In the routine analytical condition, a primary $^{133}\text{Cs}^+$ beam with an intensity of ~ 1.6 nA was focused to a $10\text{-}\mu\text{m}$ diameter with a Gaussian density distribution. The dish-shaped SIMS analysis pits formed by the Gaussian focused beam have a depth of 1 to $2\ \mu\text{m}$. The standard UWPY-1 (Ushikubo et al., 2014) was used as a bracketing standard to monitor instrument stability and analytical spot-to-spot reproducibility. Grains of UWPY-1 were cast in the center of each sample mount and were measured in at least four spots before and after every 10 to 12 analyses. Measured ratios of $^{34}\text{S}/^{32}\text{S}$ were reported in delta notation ($\delta^{34}\text{S}$) relative to the Vienna Canyon Diablo troilite (VCDT). For $\delta^{34}\text{S}$, a correction factor was determined for each of the UWPY-1 brackets by comparing the average measured value of the standard with its known value (16.04‰ VCDT). The precision of the S-isotope analyses in this study, reported at the level of two standard deviation (2SD) varies between 0.05 and 0.4‰. For chalcopyrite, Trout Lake chalcopyrite ($\delta^{34}\text{S}$: 0.3‰; Crowe and Vaughan, 1996) was used for estimating instrumental mass bias as a relative bias to UWPY-1 (−4.3‰) in the session.

Bulk IRMS sulfur isotope analysis

Bulk sulfur isotope analyses were conducted at the Department of Geological Sciences, Queen's University, Kingston, Ontario. The weight range for samples varied between 0.3 and 1.05 mg for pyrite and chalcopyrite. Anhydrite samples weighed between 0.71 and 1.12 mg. The sample size was set to guarantee a minimum amount of sulfide or sulfate minerals consistent with the purity of the sample. The sulfur isotope composition for sulfides and anhydrite was measured using a MAT 253 isotope ratio mass spectrometer coupled to a Costech ECS 4010 element analyzer. The $\delta^{34}\text{S}$ values were

calculated by normalizing the $^{34}\text{S}/^{32}\text{S}$ ratios relative to VCDT international standard, expressed in delta ($\delta^{34}\text{S}$) notation. Total uncertainties are estimated to be better than $\pm 0.2\text{‰}$ for $\delta^{34}\text{S}$. Bulk trace element analyses of the same pyrite grains measured by IRMS were performed using ICP-MS. The ICP-MS analyses were conducted at Queen's University using an Finnigan MAT Element ICP-MS. The minerals analyzed were handpicked from the same samples analyzed for bulk sulfur isotope analyses. The weight range for samples varied between 30.2 and 121.7 mg. Samples were digested using aqua regia, and reference materials CCu-1C and PTC-1 were measured along with the samples to ensure quality assurance and quality control.

Results

Textural relationships and paragenesis of pyrite samples

Pyrite from the Candelaria-Punta del Cobre district is mostly either subhedral to euhedral, is partly skeletal, and forms relatively large grains, varying in size from ~ 2 to ~ 0.5 mm across. BSE images of pyrite grains reveal a granular texture around their border, suggesting growth of younger pyrite crystals with minor chalcopyrite around early euhedral grains (Fig. 3A, B, D). Some pyrite grains contain minor inclusions of chalcopyrite and magnetite (Fig. 3A, C). A complete description of the mineral assemblages for each sample is presented in Table 1.

Pyrite grains from group 1 (samples DH996-23, DH996-21, ES032-15, and AD0066-26; Fig. 3D, H) are part of a magnetite \pm actinolite \pm biotite \pm K-feldspar pervasive alteration assemblage with complete texturally destructive replacement of primary mineralogy. This assemblage contains chalcopyrite and minor pyrrhotite, which is only present in samples from the manto horizon. Pyrite grains from group 2 (samples DH996-2, ES032-5, and AD0093-14; Fig. 3A, E) occur with more heterogeneous mineral assemblages. Samples DH996-2 and AD0093-14 exhibit patchy magnetite \pm actinolite \pm biotite \pm K-feldspar with minor chalcopyrite. Sample ES032-5, closer to the contact with the Copiapó batholith, is characterized by a pervasive garnet-diopside-actinolite-K-feldspar-scapolite alteration assemblage, with minor magnetite \pm specularite \pm chalcopyrite. Samples with late veins in group 3 include LD1493-9 (Fig. 3B, F), where pyrite occurs \pm magnetite \pm actinolite \pm K-feldspar, AD0357-3, AD0357-8, AD0357-10, and AD009-14 with pyrite in anhydrite-chalcopyrite-pyrite-epidote veins. The latter group of samples are all from the Alcaparrosa deposit, but similar veins occur in many of the deposits in the Punta del Cobre district. Finally, pyrite grains from sample LP-1 (group 4) are dominated by magnetite \pm biotite \pm K-feldspar \pm specularite with chalcopyrite (Fig. 3C, G).

Chemical zonation of pyrite

The distribution of Se, As, Ni, and Co within pyrite grains from the Candelaria-Punta del Cobre district was determined by collecting synchrotron $\mu\text{-XRF}$ data for individual grains and generating elemental maps (Figs. 4–7). These elemental maps show chemical zonation and heterogeneities at the grain scale for different trace elements in pyrite (e.g., core vs. rim), and allow comparisons among samples throughout the district and mineralization stages. The elements that display the most

significant variations at the grain scale are Ni, As, Se, and Co, and are described below for each unit.

Pyrite grains in samples from group 1, specifically those from mineralized bodies within the manto stratigraphic horizon in Candelaria and Alcaparrosa (ES032-15 and AD066-26, respectively; Fig. 4A, B) display a distinct zonation of Ni and As, where contents are higher in the core, with concentrations up to ~1 wt % and 500 ppm, respectively. Selenium contents display little zonation, although the concentration varies irregularly in some parts of individual pyrite grains (up to ~100 ppm). The concentration of Co is low (~<100 ppm) in all of the pyrite samples from the manto horizon. The remaining pyrite grains from group 1 (from fault-hosted orebodies; samples DH996-23, DH996-21, and LD1493-9; Fig. 4C, D), are zoned. In these samples the Co content is inversely correlated with Ni and Se; i.e., zones with high Co contents have low Ni and Se contents, and other zones contain elevated Ni and Se concentrations and low Co contents. The distribution of As is more erratic, having a positive correlation with Ni in sample DH996-21 and the opposite in sample DH996-23.

Pyrite samples from group 2 are zoned, but chemical zoning varies among the samples (Fig. 5). Samples ES032-5 and AD0093-14 display a negative correlation between Ni and Co and a positive correlation between Ni and Se, and both samples contain less Se than samples from group 1. Sample AD0093-14 has a grain with a Co-rich core and another grain with a Ni-rich core and Co-rich rim (Fig. 5C). Sample ES032-5 contains pyrite aggregates that include grains with elevated Ni and low Co contents and grains with the opposite. The As

contents in samples ES032-5 and AD0093-14 are lower than in samples from group 1 and display a weak negative correlation with Se. Sample DH996-2 contains grains showing a positive correlation between As and Co and a strong negative correlation between Co and Se, which is not observed in the other two samples.

Pyrite from the group 3 sample, LD1493-9 (Fig. 6), displays a zonation pattern with Ni and As concentrated in the cores of grains and the Co content increasing toward the rim of the pyrite grains and aggregates. Selenium contents in this sample are low (~<15 ppm).

Pyrite grains in group 4 sample, LP-1 (Fig. 7), show strong elemental zonation. The core and outer rim of the largest grain in this sample have high Co (more than 1%) and very high Se contents (up to 200 ppm), reflecting a strong positive correlation between Co and Se. The As content is highest in the outermost rim where little Ni was detected (~<50 ppm).

Major, minor, and trace element geochemistry of pyrite

A total of 185 points in pyrite were measured for 58 elements (Ca, Sc, Ti, V, Cr, Mn, Fe, Co, Ni, Cu, Zn, Ga, Ge, As, Se, Rb, Sr, Y, Zr, Nb, Mo, Ag, Cd, In, Sn, Sb, Te, Cs, Ba, rare earth elements, Hf, Ta, W, Pt, Au, Hg, Tl, Pb, Bi, Th, U). A statistical summary is presented in Table 2, and the data for elements with significant concentrations are provided in Appendix Table A1. LA-ICP-MS and EPMA analytical values obtained from the same pyrite grains vary between 2 and 10%, which is well within the variation attributed to the heterogeneous nature of the pyrite grains, especially considering

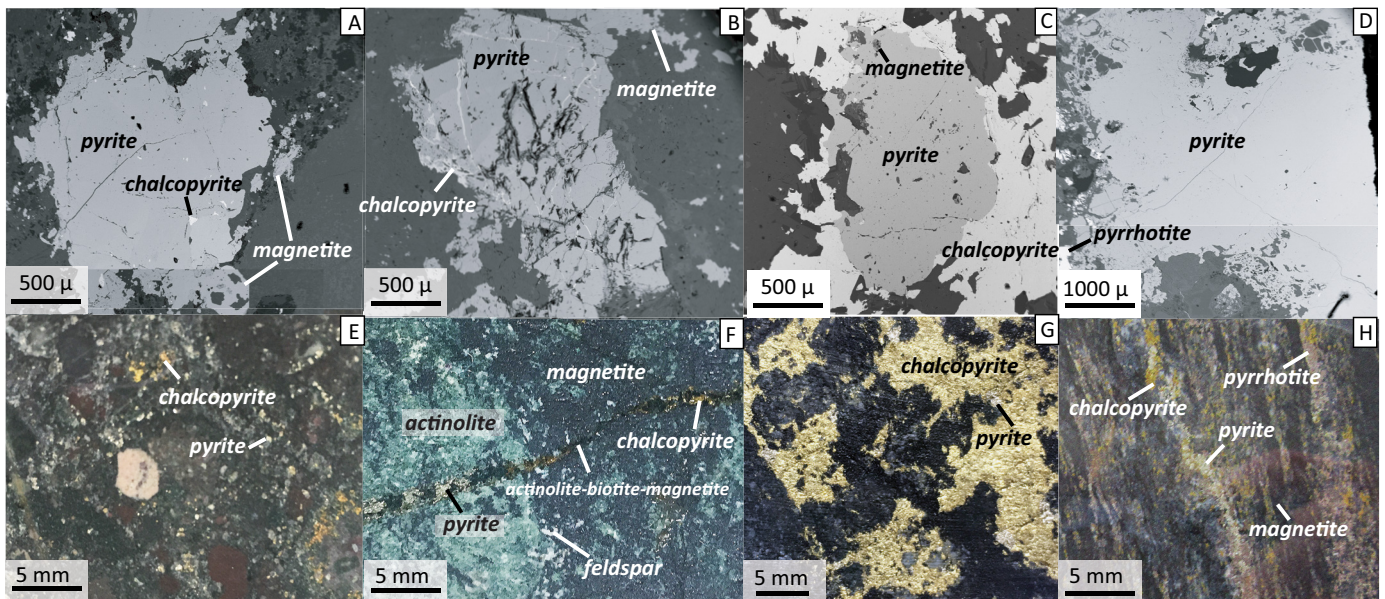


Fig. 3. BSE (A-D) and hand sample photos (E-H) of representative pyrite-bearing samples. (A) Sample DH996-2, euhedral pyrite with pyrite regrowth on the edge of the main grain and chalcopyrite inclusions. (B) Sample LD1493-9, euhedral pyrite from a vein with pyrite and chalcopyrite regrowth on the edge of the main grain. (C) Sample LP-1, euhedral pyrite surrounded by chalcopyrite and with minor magnetite inclusions. (D) Sample ES032-15, euhedral pyrite with pyrite regrowth on the edge of the main grain. (E) Hand sample of sample DH996-2, pyrite and chalcopyrite are disseminated in the volcanic-sedimentary unit of the Punta del Cobre Formation. (F) Hand sample LD1493-9, pyrite-chalcopyrite-actinolite-magnetite vein cutting main-stage actinolite-magnetite-K-feldspar pervasive alteration in the lower andesite of the Punta del Cobre Formation. (G) Hand sample of sample LP-1, chalcopyrite-pyrite mineralization in the Abundancia Formation (lower part of the Chañarcillo Group). (H) Hand sample of sample ES032-15, pyrite-chalcopyrite-pyrrhotite mineralization with pervasive magnetite-biotite-K-feldspar-actinolite alteration in the volcanic-sedimentary unit of the Punta del Cobre Formation.

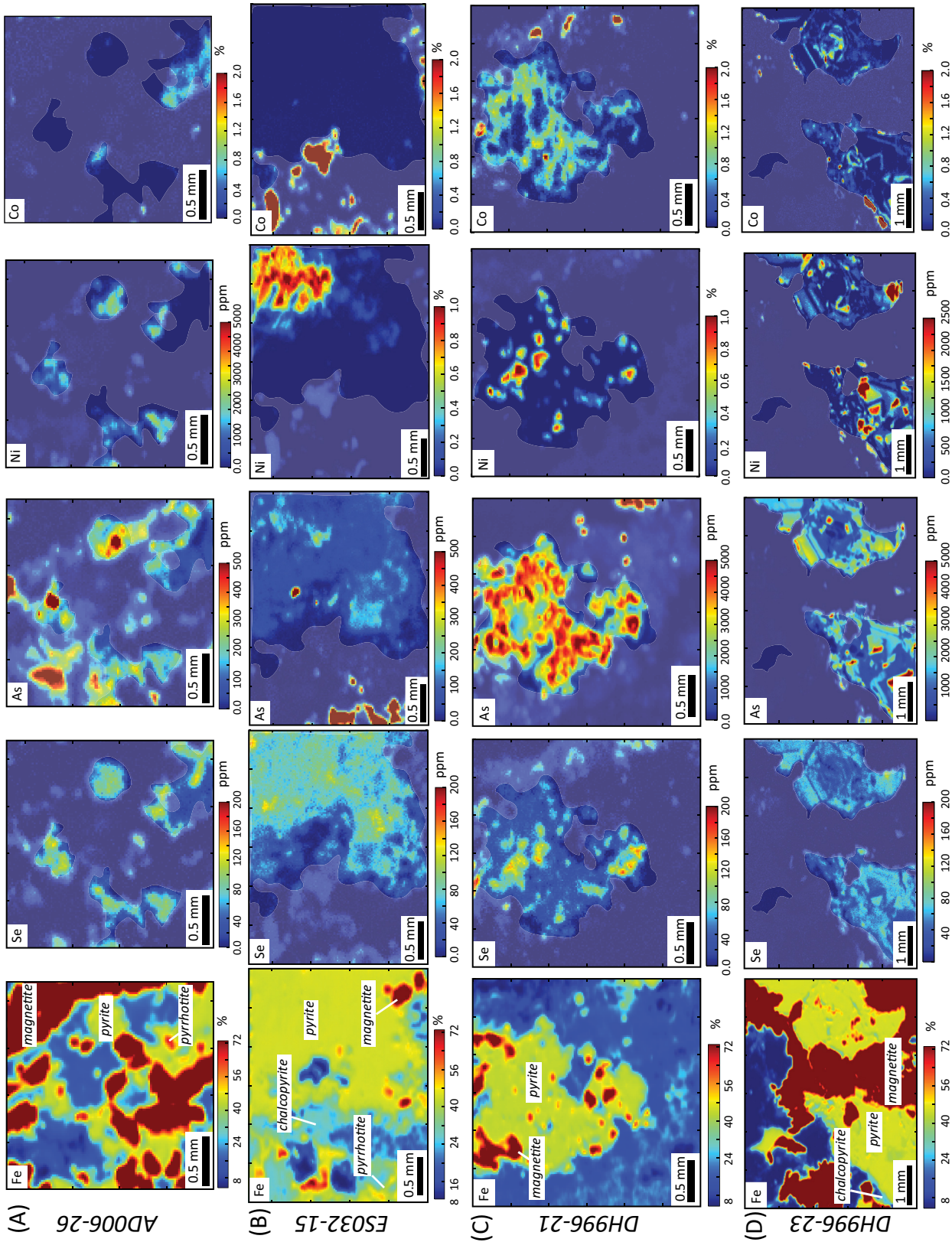


Fig. 4. Synchrotron-XRF element maps for pyrite samples from group 1. (A) Sample AD0066-23, disseminated pyrite, pyrrothite, and magnetite from the mantle horizon in Alcaparrasa. (B) Sample ES032-15, pyrite grain surrounded by disseminated chalcopyrite, pyrrothite, and magnetite from the mantle horizon in Candalaria. (C) Sample DH996-23, pyrite grain with magnetite from structurally controlled orebody in the Santos deposit. (D) Sample DH996-21, aggregate of pyrite grains contained in a vein with magnetite and minor chalcopyrite from structurally controlled orebody in the Santos deposit. Areas of the image that do not include pyrite have been covered in order to focus attention to elemental variation in pyrite.

that each analytical method analyzed a slightly different spot within the pyrite grains. Evaluation of the data focused on trace and minor elements with significant and consistent concentrations in the pyrite samples (e.g., Co, Ni, Cu, Zn, Pb, As, Sb, Se, Ag, and Cd). The Au data were discarded as the LA-ICP-MS analyses were carried out after the SIMS measurements, which had been coated with Au as part of the analytical procedure.

Boxplot diagrams of the combined LA-ICP-MS and EPMA data set (Fig. 8) show significant variations in most elements with the exception of Zn and Cu, where all samples display a similar range of values. Samples from group 1 (Fig. 8) have a similar range of Cu, Ni, As, Se, Ag, and Cd values, but sample ES032-15 (from the manto horizon) has higher values of Pb and Sb contents than other samples. Pyrite samples from group 2 (Fig. 8) have Pb, Sb, and Cd values similar to those of sample DH996-2, also showing more variation in the concentration of most elements, especially Co, Se, As, and Ag. Sample ES032-5 has higher Ni and lower Co concentrations than the other two samples from group 2. Group 3 sample LD1493-9 has elevated Pb, Sb, and Ag values compared to all other samples (Fig. 8). Group 4 sample LP-1 (Fig. 8) has the highest concentrations of Co and Se in the full data set but low Ni and Pb concentrations, and Cd is below detection.

Bulk analysis of pyrite in late veins from group 3 returned similar Se contents, whereas Ni varies from ~500 (sample AD009-14) to ~3,000 ppm (sample AD357-10). Cobalt varies from ~70 (sample AD357-8) to 400 ppm (sample AD00914), and As is consistently low (<16 ppm) (Table 3). Sample AD357-3 has Zn, Se, and Ni contents similar to those of sample AD0093-14 but lower As and Co contents.

On a comparative basis for the complete data set, pyrites from group 1 manto samples are enriched in Sb while pyrite from late vein samples are enriched in Pb and Ag and depleted in Se. The pyrite sample from the base of the Chañarcillo Group (LP-1, group 4) in Las Pintadas deposit displays different characteristics from the rest of the sample set, with the highest Co and Se contents and the lowest Pb and Cd contents.

Stable sulfur isotope composition of pyrite

In situ $\delta^{34}\text{S}$ values were determined on the same pyrite samples that were analyzed by synchrotron-XRF, EPMA, and LA-ICP-MS. The results show a range of values from ~-2 to ~10‰ (Fig. 9A; statistical summary in Table 2 and the whole data set in App. Table A2). The majority of the measured values range between ~-1 and 2‰. The $\delta^{34}\text{S}$ values calculated from in situ SIMS measurements on chalcopyrite grains adjacent to some of the pyrite grains display a similar range of values (Fig. 9B). Four pyrite samples have homogeneous sulfur isotope compositions (Fig. 10A, B, E, I), while the rest display clear microscale variations; e.g., the $\delta^{34}\text{S}$ values of sample DH996-2 vary by 4‰ over <1 mm (Fig. 10F).

Pyrite samples from the manto horizon, group 1, display values between -2 and 2‰ and are homogeneous, with the majority of $\delta^{34}\text{S}$ values between 1 and 1.5‰ (Fig. 10A-D). Samples from group 2 have heterogeneous $\delta^{34}\text{S}$ values (Fig. 10F-H) with different samples showing different degrees of variation: sample DH996-2 -2.5 to 2.2‰, sample ES032-5 -0.95 to 2.75‰, and sample AD0093-14 3.5 to 7.3‰. Pyrite

grains from group 3 samples display homogeneous $\delta^{34}\text{S}$ values that range between 9.4 and 10.06‰, and sample LP-1 from group 4 is also homogeneous but with different $\delta^{34}\text{S}$ values, 1.17 to 2.1‰ (Fig. 10I).

The majority of the heterogeneous samples show an isotopic zonation with increasing $\delta^{34}\text{S}$ values from core to rim. Samples that are composed of aggregates of small pyrite grains (samples DH996-21 and ES032-5) display isotopic values that fluctuate, increasing and decreasing within a single transect. Chalcopyrite $\delta^{34}\text{S}$ values (depicted in blue in Fig. 10) correlate with the isotopic signature of the pyrite grains in the same sample (Fig. 10B, D, E, G, H). Bulk $\delta^{34}\text{S}$ analyses obtained by Marschik and Fontboté (2001b) on chalcopyrite from the district overlap with those obtained for this study (depicted in gray, Fig. 9B). Bulk $\delta^{34}\text{S}$ analyses were carried out on pyrite, chalcopyrite, and associated anhydrite from late veins, all of which appeared to be in textural equilibrium. The results provide sulfide $\delta^{34}\text{S}$ values for pyrite and chalcopyrite of 4 to 12.5‰ and sulfate $\delta^{34}\text{S}$ values for anhydrite of 16 to 21.4‰. (Table 3). The higher $\delta^{34}\text{S}$ values in this group overlap with those from pyrite in the late vein sample LD1493-9.

Discussion

Evaluation of trace element signatures

Despite its simple formula, pyrite can effectively incorporate numerous trace metals in its structure, both in solid solution and as nanoparticles (Reich et al., 2005, 2013; Deditius et al., 2009, 2011). Characterizing trace element variations within pyrite can serve as a monitor for changes in the hydrothermal fluid evolution (e.g., Huston et al., 1995b; Large et al., 2009; Reich et al., 2013, 2016; Gregory et al., 2015; Tardani et al., 2017). These variations can be attributed to (1) changes in temperature of the hydrothermal fluid and the partitioning of trace elements between coexisting mineral phases at different temperatures (Abraitis et al., 2004; Keith et al., 2016), (2) changes in the redox and H^+ activity conditions with the solubility of trace elements decreasing or increasing at different f_{O_2} and pH, respectively (Thomson et al., 1993; Keith et al., 2017), and/or (3) changes in the composition of the hydrothermal fluid that will be reflected in the pyrite chemistry (Huston et al., 1995a; Abraitis et al., 2004; Tardani et al., 2017).

Hydrothermal alteration mineral assemblages within the Candelaria-Punta del Cobre district are relatively consistent both vertically and horizontally. The main alteration event from depth to the manto horizon consists of iron-rich calc-potassic mineral assemblages dominated by magnetite-biotite-K-feldspar-actinolite (del Real et al., 2018). At higher stratigraphic horizons, alteration changes from magnetite to specularite dominant, and sodic-calcic alteration minerals such as albite-garnet-diopside-scapolite-amphibole are concentrated in rocks of the upper andesite unit and units at the base of the Chañarcillo Group, especially close to the Copiapó batholith (Marschik and Fontboté, 2001b; del Real et al., 2018). The relative lack of distinct variations in the alteration assemblages and paragenesis suggests that pH changes in the hydrothermal fluids generally, or during fluid-wall-rock reactions, were not spatially or temporally significant. Alteration mineralogy suggests a near-neutral pH for the hydrothermal

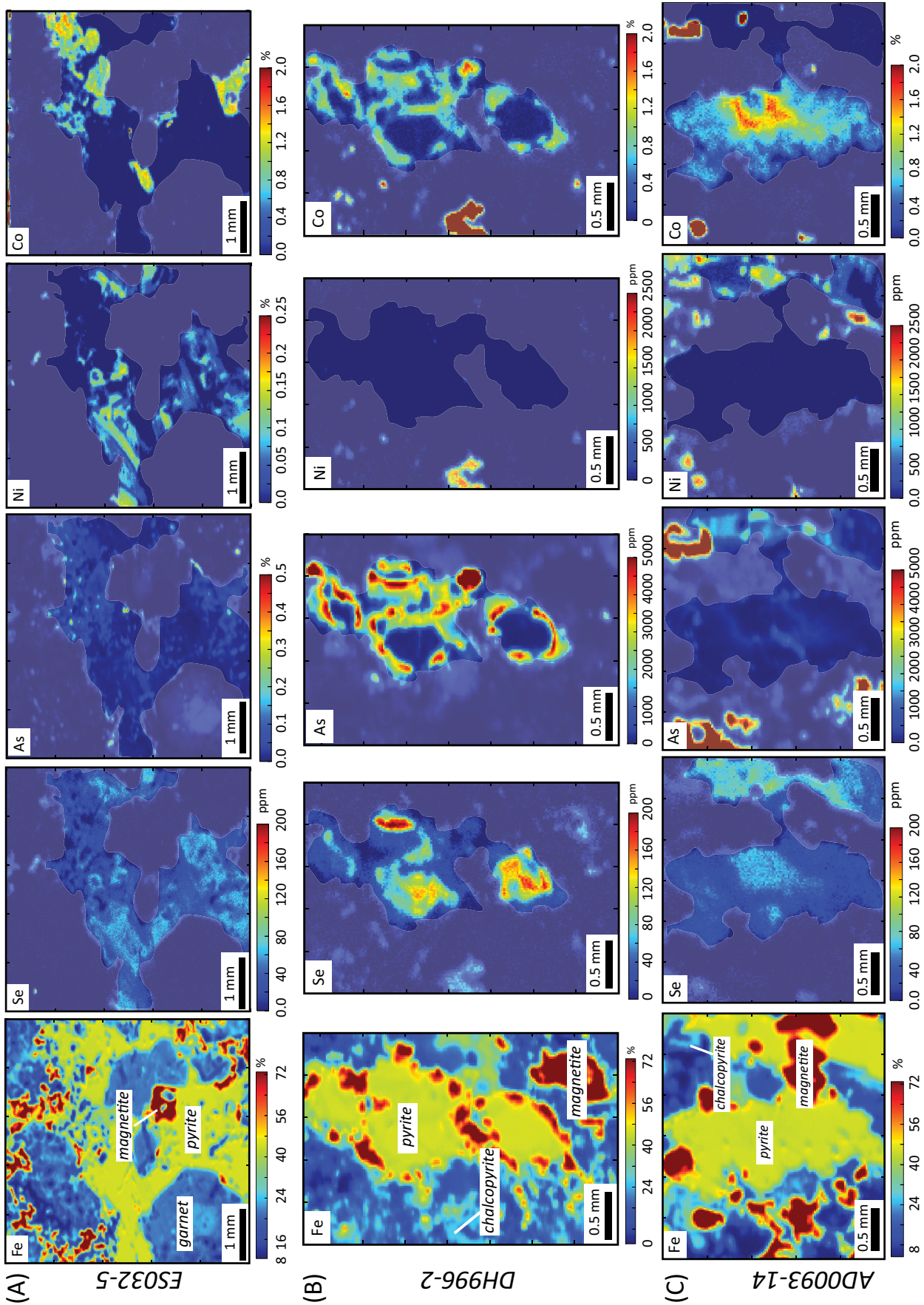


Fig. 5. Synchrotron-XRF element maps for pyrite samples taken from group 2. (A) Sample ES032-5, aggregate of pyrite grains with garnet and magnetite from upper andesite unit above de Candelaria deposit. (B) Sample DH996-2, pyrite grain with magnetite and chalcopyrite from above the dacite dome unit in the Santos deposit. (C) Sample AD0093-14, pyrite grains with magnetite and minor chalcopyrite from dacite dome unit in the Alcaparrosa deposit. Areas of the image that do not include pyrite have been masked in order to focus attention to elemental variation in pyrite.

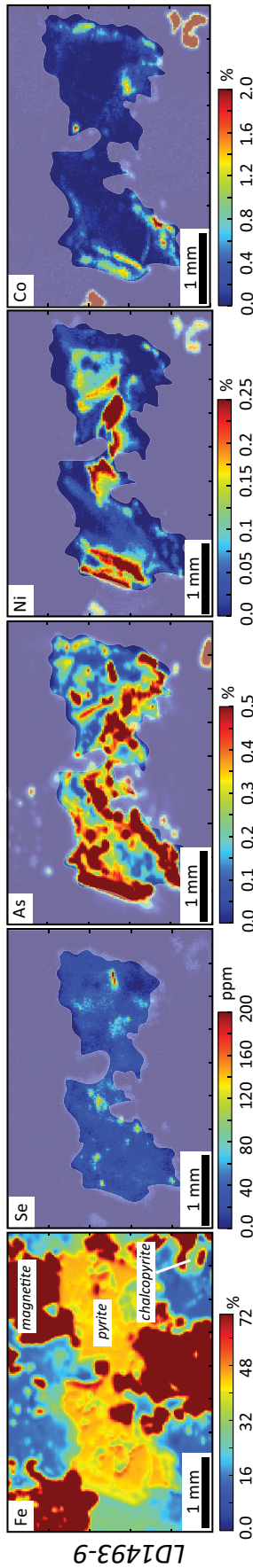


Fig. 6. Synchrotron-XRF element map for pyrite samples taken from late vein sample LD1493-9, an aggregate of pyrite grains contained in a vein with chalcopyrite (not pictured) surrounded by disseminated magnetite and chalcopyrite. This vein sample cuts the main mineralization in the Candelaria deposit. A layer of opacity was added in order to delimit the pyrite grains in the trace element maps.

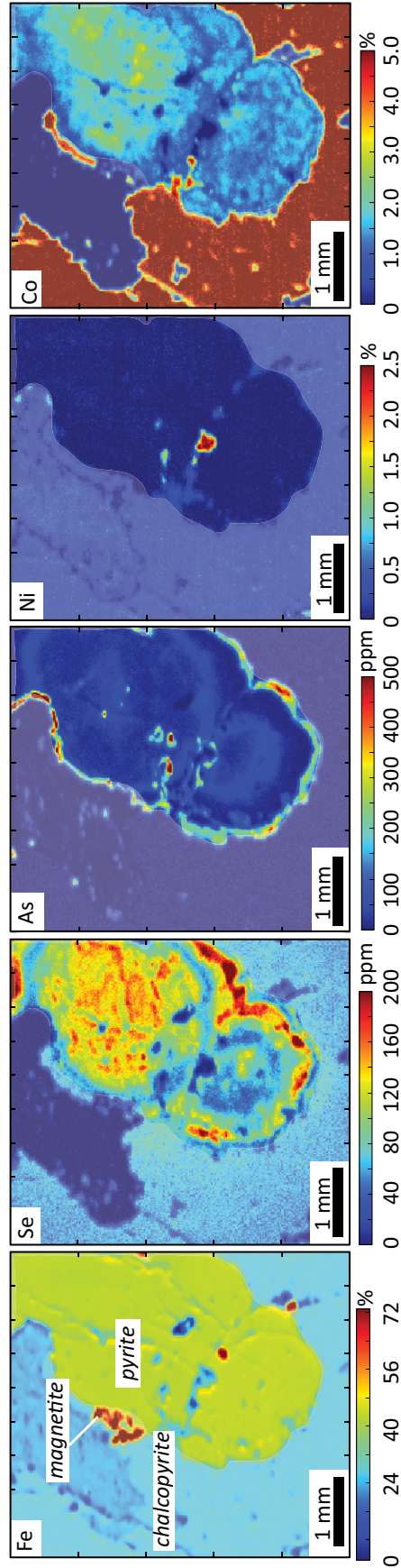


Fig. 7. Synchrotron-XRF element maps for pyrite sample from group 4. Sample LP-1 was taken from the base of the Chañarillo Group (Abundancia Fm) from Las Pintadas deposit. A large pyrite grain is surrounded by chalcopyrite and minor magnetite. Areas of the image that do not include pyrite have been masked in order to focus attention to elemental variation in pyrite.

LD1493-9

Table 2. Statistical Average Values for $\Delta^{34}\text{S}$ (‰) and Trace Elements (ppm) for Pyrite Samples

Sample	<i>n</i>	$\delta^{34}\text{S}$	2SD	Co	Ni	Cu	Zn	Pb	As	Sb	Se	Ag	Cd
ES032-15	38	1.33	0.28	1,191.36	5,045.09	83.48	7.18	38.46	120.38	22.35	71.70	0.59	0.11
AD006-26	9	1.52	0.12	2,664.30	2,458.43	475.54	29.85	2.37	355.49	0.06	44.55	2.30	0.06
DH996-21	28	-0.14	0.07	6,923.98	1,851.16	1,434.02	7.62	18.54	2,361.96	0.46	73.06	3.88	0.05
DH996-23	16	0.03	0.31	15,090.33	2,400.17	915.40	17.20	15.25	7,127.38	0.63	73.05	33.93	0.18
LD1493-9	14	9.60	0.14	4,707.15	2,377.69	6,444.97	14.83	821.36	3,442.11	1.48	16.85	24.85	0.03
DH996-2	22	-0.94	0.18	3,239.36	27.06	127.08	6.27	10.60	953.99	0.19	27.17	2.42	0.11
ES032-5	14	-0.15	0.40	504.38	1,440.12	829.36	55.71	302.65	209.87	0.28	42.08	9.71	0.72
AD0093-14	17	4.20	0.06	12,368.52	119.29	51.36	13.85	46.25	134.05	0.28	36.83	1.28	0.07
LP-1	27	1.44	0.14	18,348.89	56.86	31.10	3.35	0.41	236.63	0.03	100.21	0.93	-

Note: As some of the samples are zoned, some values within these grains can deviate from the numbers presented here; dash in otherwise-empty cell indicates no data available

Table 3. $\Delta^{34}\text{S}$ Isotope Values (‰) and Element Concentrations (ppm) for Whole Pyrite, Chalcopyrite, and Anhydrite Grains in Equilibrium

Sample	Mineral	Lithology	$\delta^{34}\text{S}$	Co	Ni	Cu	Zn	As	Se
AD0357-10	Pyrite	Lower andesite	7.7	232.54	3,161.83	1,770.12	155.24	5.55	11.95
AD0357-10	Anhydrite		18.1	-	-	-	-	-	-
AD0357-8	Pyrite	Lower andesite	-	71.44	1,144.20	4,077.53	52.42	7.78	20.62
AD0357-8	Chalcopyrite		6.5	-	-	-	-	-	-
AD0357-8	Anhydrite		17.7	-	-	-	-	-	-
AD0357-3	Pyrite	Dacite dome	4	121.58	722.74	4,057.00	40.03	16.92	20.84
AD0357-3	Anhydrite		16	-	-	-	-	-	-
AD009-14	Pyrite	Lower andesite	12.5	436.53	535.07	996.95	38.96	3.96	14.76
AD009-14	Anhydrite		21.4	-	-	-	-	-	-

Note: dashes in otherwise-empty cells indicate no data available

fluids (Marschik and Fontboté, 2001b). Given this conclusion, the following discussion focuses on potential changes in temperature, fluid composition, and redox conditions as factors that may have affected pyrite chemistry and sulfur isotope variation.

Significant variation of Se, As, Ni, and Co is observed among samples and within individual pyrite grains from the Candelaria-Punta del Cobre district (Figs. 4–7). Variations of other elements such as Pb and Sb are present in specific samples (Fig. 8), and we attribute these largely to small-scale inclusions (Abraitis et al., 2004). Although there is no significant variation of the alteration paragenesis in the district, the chemical zonation observed in pyrite from most samples suggests that the changes in the conditions of the hydrothermal fluid involved multiple events, at least at a local scale. Although mineral grain kinetic effects can influence mineral growth and chemical zoning (Jamtveit, 1991; Putnis et al., 1992), these are not considered important for variations in pyrite chemistry in this study because no quasi-cyclic zoning (or oscillatory zoning) in the chemical composition was observed in any of the samples used in this study (Figs. 4–7).

Selenium is able to substitute stoichiometrically for S in the pyrite structure. Several researchers have noted increasing Se concentration in pyrite with an increase in temperature (Huston et al., 1995b; Revan et al., 2014; Krumm et al., 2015; Keith et al., 2017) or a rise in f_{O_2} (Huston et al., 1995b; Large et al., 2014). Selenium varies significantly in the pyrite samples, but in most cases, it has a general positive correlation with Ni (Fig. 11A). Since incorporation of Ni into pyrite tends to be more efficient at higher-temperature conditions, the positive

Ni-Se correlation suggests that the incorporation of Se in pyrite may also be at least partly controlled by temperature (Lehner et al., 2006).

Arsenic may substitute for S nonstoichiometrically in the pyrite structure—a process requiring the substitution of ions of differing net charge polarity. The incorporation of As into the pyrite lattice may lead to distortion of the pyrite structure, increasing defect formation (Abraitis et al., 2004). Structural distortion may allow other trace elements to enter the pyrite structure, resulting in a positive correlation between As and other trace elements (e.g., Griffin et al., 1991). Arsenic concentration in pyrites analyzed in this study does not correlate with Ni or Se, but in some of the pyrite grains there is a positive correlation between Ni and Co (e.g., samples DH996-2 and DH996-23; Figs. 5, 6, 11B). Samples AD0093-14 and LP-1, however, are distinctly different, with no As-Co correlation and highly elevated Co contents. Based on the available data in this study, the As content in pyrite does appear to provide exclusive control on the concentration of other trace elements.

A positive correlation between As and Co is expected when the hydrothermal fluid contains both elements (Abraitis et al., 2004), and therefore, the lack of correlation between Co and As, as observed in samples AD0093-14 and LP-1, suggests a decoupling of these elements. This decoupling would potentially be associated with changes in the composition and/or nature of the hydrothermal fluid, as has been proposed for Cu and As in high-sulfidation systems (Deditius et al., 2009; Tardani et al., 2017). Sample LP-1 (group 4) from the main mineralization event in Las Pintadas deposit has well correlated

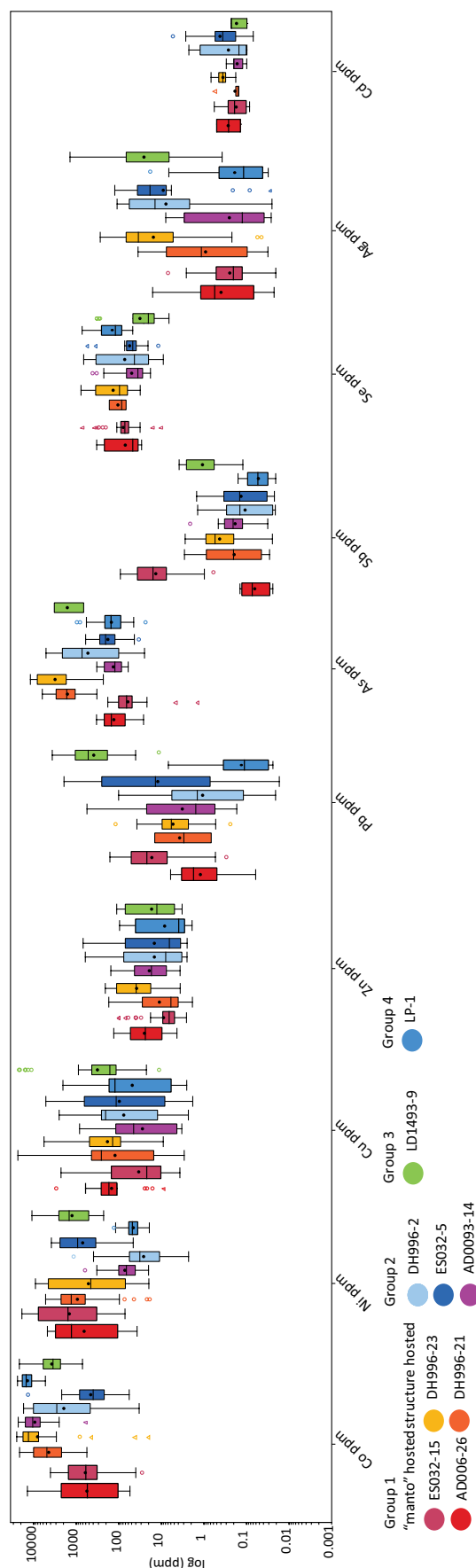


Fig. 8. Box and whisker plot showing trace element concentrations determined by LA-ICP-MS integrated with EPMA. Cd was under detection limit in sample LP-1. The central box represents 50% of data from quartile 1 (Q1) to quartile 3 (Q3); outlier circles and triangles indicate the data that is farther than 1.5 (Q3-Q1) from the box. The whiskers include the extreme outlier values.

Co and Se contents compared to the rest of the sample set, together with lower Ni concentrations (Table 2). Las Pintadas deposit is ~5 km south of the main cluster of IOCG deposits in the Punta del Cobre district (Fig. 2) and is hosted at the base of the Chañarcillo Group, at a higher stratigraphic level than the other major deposits. The differences in the pyrite chemistry suggest that the hydrothermal fluid responsible for mineralization in Las Pintadas may have had a distinct composition compared to IOCG mineralization in the rest of the district. Sample AD0093-14 from group 3 is hosted the dacite dome unit above the manto horizon in the Alcaparrosa deposit, and therefore, it seems unlikely that pyrite grains in this sample formed under identical conditions to those for sample LP-1 at Las Pintadas. The decoupling of As and Co in both samples, however, suggests that some similar processes influenced incorporation of As and Co in pyrite in both areas.

Co and Ni concentration and Co/Ni ratios

Both Co and Ni may substitute stoichiometrically for Fe in pyrite, reflecting the fact that Co^{2+} and Ni^{2+} have a similar ionic radius to Fe^{2+} (Tossell et al., 1981; Abraitis et al., 2004). The Co and Ni concentrations reported here for pyrite from the Candelaria-Punta del Cobre district are considerably higher than in other hydrothermal systems, including porphyry copper deposits and epithermal Au-Ag systems (Reich et al., 2013; Deditius et al., 2014; Franchini et al., 2015), with samples from the manto horizon having Ni concentrations locally >1 wt % (Fig. 8). The concentration of Co and Ni is higher in mafic magmas than in intermediate magmas (Taylor et al., 1969; Nicholls et al., 1980; Rudnick and Taylor, 1987; Longhi et al., 2010; Nadeau et al., 2010) and significantly higher than felsic magmas (Gülaçar and Delaloye, 1976; Zhao et al., 2011). Therefore, the andesitic and dacitic volcanic host rocks of the Punta del Cobre Formation are an unlikely source for the high Ni and Co concentrations observed in pyrite. The Ni-Co contents are most likely derived from deep mafic rocks via hydrothermal leaching or magmatic-hydrothermal fluids released from mafic magmas.

Variations in Co/Ni ratios in pyrite have been used as a proxy for classifying the origin and source of hydrothermal mineral deposits, since both elements may be incorporated equally, conserving the ratio in associated hydrothermal fluids (e.g., Bralía et al., 1979; Campbell and Ethier, 1984; Bajwah et al., 1987; Large et al., 2009; Koglin et al., 2010; Reich et al., 2016). Previous research using Co/Ni ratios determined that low Co/Ni ratios (<1) are characteristic of pyrite in mineral deposits that formed at or below the seafloor in sedimentary and volcanic settings (Bralía et al., 1979), and Co/Ni ratios between ~1 and 10 are characteristic of magmatic-hydrothermal deposits (Bajwah et al., 1987; Reich et al., 2016).

The relatively restricted range of Co/Ni ratios of pyrite from the Candelaria-Punta del Cobre district suggests incorporation from a fluid of a similarly restricted ratio. Minor changes in the Co/Ni ratio from core to rim in pyrite from some samples (e.g., DH996-23) are not sufficient or uniform enough to suggest broad changes in fluid composition. The dominant range of Co/Ni ratios between ~1 and 10 (Fig. 12) is consistent with pyrite of a magmatic-hydrothermal origin as defined by Reich et al. (2016). The Co/Ni ratios higher than 100 occur in pyrite grains with very low Ni concentrations in samples

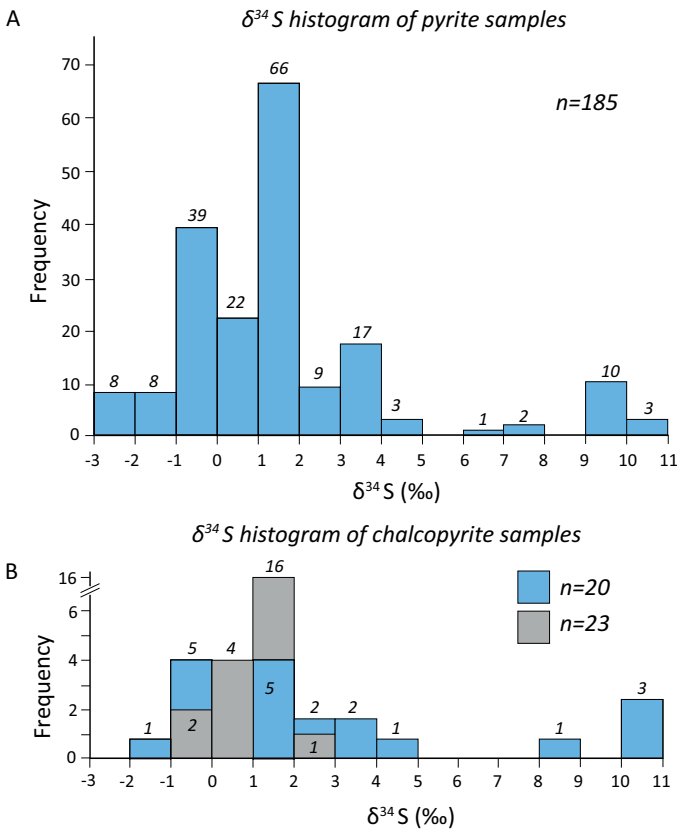


Fig. 9. $\delta^{34}\text{S}$ histogram of in situ measurements obtained from pyrite (A) and chalcopyrite (B). The highest concentration of values concentrate between -1 and 2 $\delta^{34}\text{S}$. Samples depicted in gray correspond to analysis carried out by Marschik and Fontboté (2001b).

from higher stratigraphic levels (e.g., LP-1 and DH996-2). The composition of wall rocks or formation at lower temperatures, both potentially consistent with their stratigraphic position, may have influenced the composition of pyrites in these samples.

The range of Co/Ni ratios from pyrite in the Candelaria-Punta del Cobre district is similar to the range found at the Mantoverde and Ernest Henry IOCG deposits (Benavides et al., 2007; Rusk et al., 2010) and at the Los Colorados IOA deposit (Reich et al., 2016). At Los Colorados, these ratios have been interpreted as an indicator of the mafic affinity for the magmatic-hydrothermal fluid source (Reich et al., 2016). A mafic magmatic source for fluids is also suggested for the Candelaria Punta del Cobre system, which is further supported by Cl isotope data indicative of a mafic- or mantle-derived origin for the hydrothermal fluids responsible for mineralization in the Candelaria deposit (Chiaradia et al., 2006).

Origin of $\delta^{34}\text{S}$ variation

The isotopic composition of sulfur in hydrothermal minerals is strongly controlled by the temperature, f_{O_2} , and pH of the hydrothermal fluids (Ohmoto, 1972; Rye and Ohmoto, 1974). The isotopic ratios of sulfur ($\delta^{34}\text{S}$) in sulfide minerals have been successfully used to interpret the origin of ore deposits (Seal, 2006, and references therein). The sulfur isotope signatures of different ore-related geologic environments range from strongly positive to strongly negative with the following breakdown: (1) marine evaporate sequences tend to display values of $\delta^{34}\text{S} > 10\text{‰}$ (Claypool et al., 1980; Strauss, 1999), (2) mantle sulfides have $\delta^{34}\text{S}$ between ~ 0 and 1.0‰ (Seal, 2006), (3) continental and island-arc basalts are similar or slightly more positive than mantle sulfides at $\delta^{34}\text{S} \sim 1.0\text{‰}$ (Ueda and

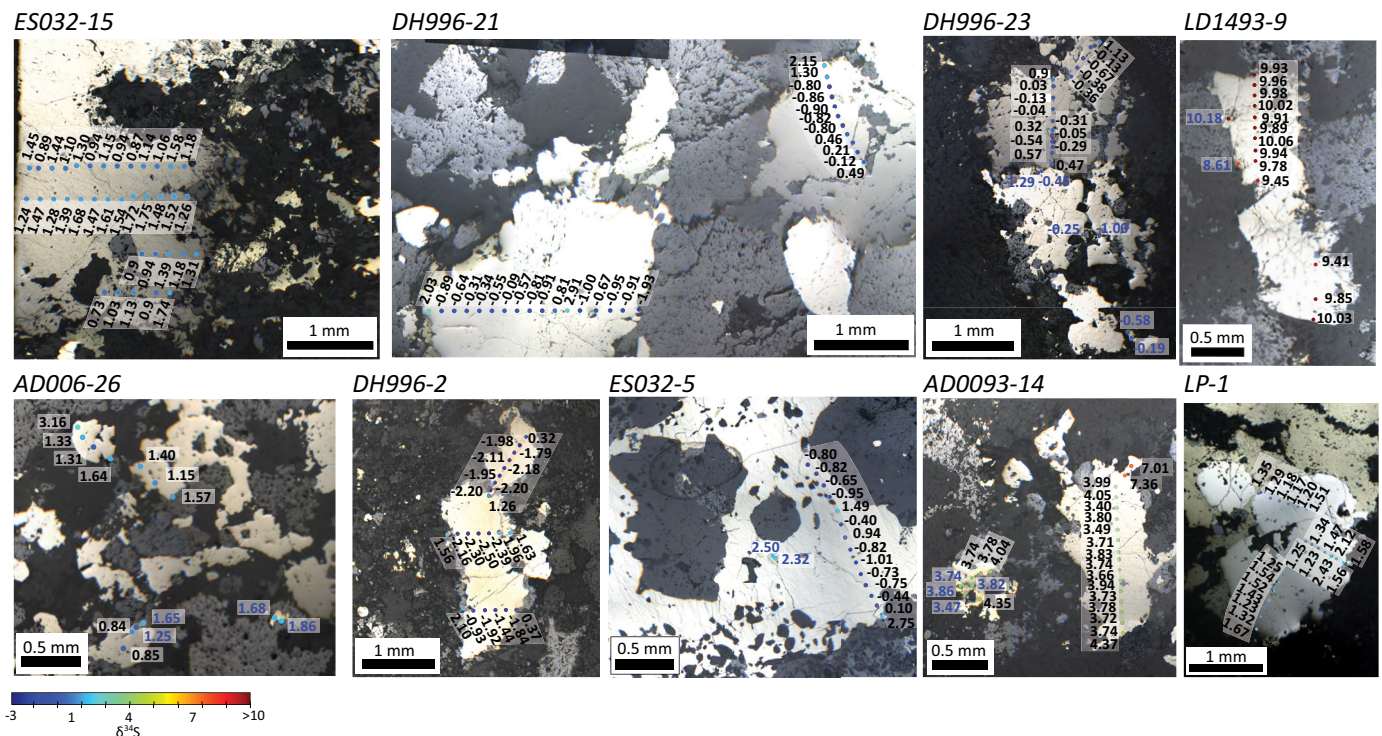


Fig. 10. $\delta^{34}\text{S}$ in situ measurements of pyrite and chalcopyrite grain samples for this study. Chalcopyrite values are depicted in blue. Point colors are based on color scale. The same points were measured using LA-ICP-MS for pyrite chemistry.

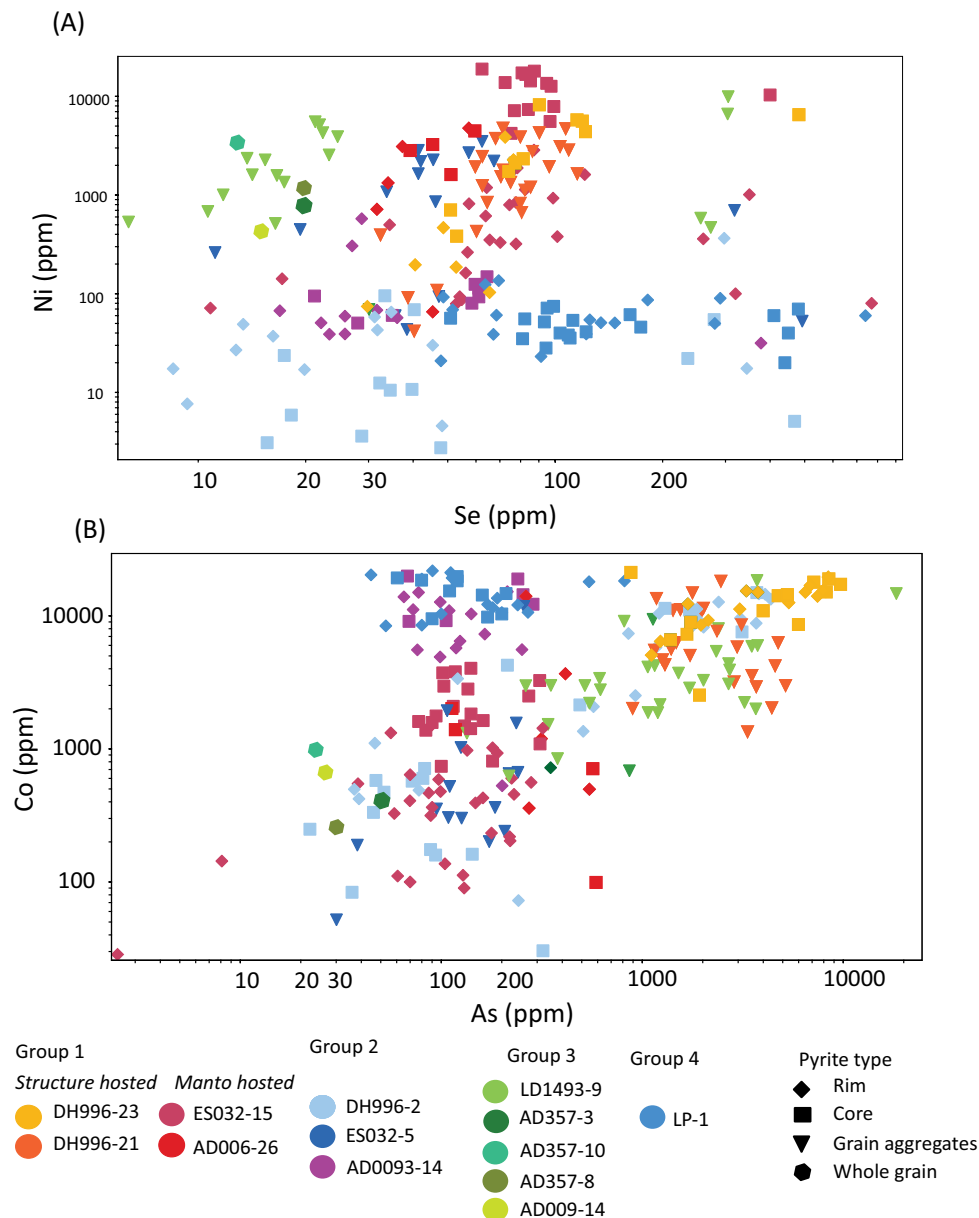


Fig. 11. Element variation diagrams from LA-ICP-MS and EPMA analysis on pyrite grains showing a positive trend between Ni and Se (A) and Co and As (B). In both diagrams data points from sample LP-1 from the main mineralization event from Las Pintadas are off the positive trend formed between the other samples, and in the diagram of As and Co sample AD0093-14 is also off trend together with LP-1

Sakai, 1984), (4) andesites typically have more positive $\delta^{34}\text{S}$ values $\sim 2.6\%$ (Rye et al., 1984), and (5) the oceanic sulfur cycle that includes euxinic black shales tends to display negative values of $\delta^{34}\text{S} < -10\%$ (Chambers, 1982; Strauss, 1997).

Although most of the $\delta^{34}\text{S}$ values for pyrite samples from the Candelaria-Punta del Cobre district concentrate between -2 and 2% , the presence of samples with values as high as 12% (Fig. 9) requires variations in fluid conditions or the source of sulfur. The limited variations within the bulk of the data may reflect minor variation in the source of S, interaction with different host rocks, or slight temperature changes. Changes in the f_{O_2} of a hydrothermal fluid would not affect the isotopic composition except when pyrite or other sulfide

minerals are in equilibrium with Fe oxides, such as magnetite and/or hematite (Ohmoto, 1972; Rye and Ohmoto, 1974). In these cases, $\delta^{34}\text{S}$ values may differ from the original $\delta^{34}\text{S}$ of the fluid source, and variations will reflect a variation in f_{O_2} of the ore-forming fluids. The Fe oxide alteration mineralogy associated with the Candelaria-Punta del Cobre deposits includes the presence of magnetite, mushketovite (specular hematite replaced by magnetite), and specular hematite, where specularite characterizes the late events and the highest levels of the hydrothermal system (Marschik and Fontboté, 2001b; del Real et al., 2018). Changes in the Fe oxide mineralogy may reflect variation in f_{O_2} and temperature conditions of the hydrothermal fluid (Ohmoto, 2003; Otake et al., 2010).

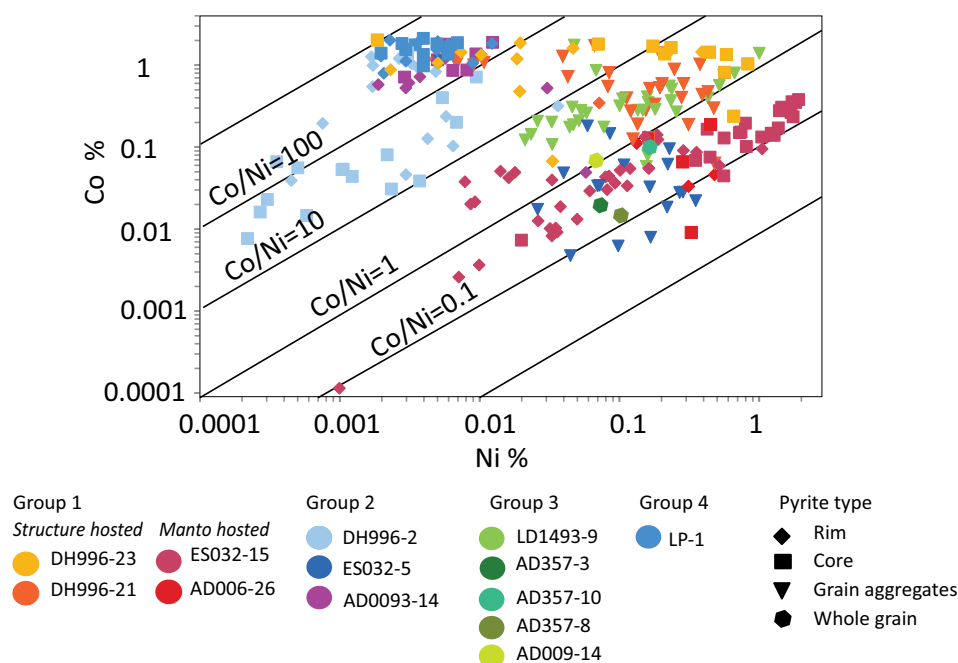


Fig. 12. Co versus Ni variation diagram and Co/Ni ratios of the pyrite measurements. The Co/Ni ratios of pyrite from the Candelaria-Punta del Cobre district determined in this study range between ~0.1 and 100, where the majority of samples range between 1 and 10, consistent with pyrite of a magmatic-hydrothermal origin. Samples with Co/Ni ~100 reflect pyrite grains with very low Ni concentrations formed at shallower stratigraphic levels.

Sulfide minerals in equilibrium with pyrrhotite are more likely to possess $\delta^{34}\text{S}$ values close to the initial $\delta^{34}\text{S}$ values of the source fluid when the temperature of mineralization is $>200^\circ\text{C}$ (Ohmoto, 1972). The mineral assemblage associated with group 1 samples from the manto horizon comprises intergrowths of chalcopyrite-pyrite-pyrrhotite-magnetite, and therefore it is likely that sulfide $\delta^{34}\text{S}$ values reflect those of the source hydrothermal fluids. Values for these samples range between ~1 and 1.5‰, consistent with a magmatic source of sulfur. Magmatic sulfur could be derived directly from a magmatic-hydrothermal fluid or by leaching magmatic sulfur from the volcanic sequence in the footwall. Pyrite Co/Ni ratios of ~1 for pyrite in samples from the manto suggest a mafic magmatic source, but this is unlikely to be from the intermediate volcanic rocks of the Punta del Cobre Formation, as discussed above. A magmatic-hydrothermal origin for the sulfur and the Co/Ni ratios of the pyrite, and by inference the mineralizing fluids, is therefore preferred. In contrast, pyrite from group 3 late vein samples LD1493-9 and AD0357-14 (anhydrite-bearing vein) show $\delta^{34}\text{S}$ values $>10\text{‰}$, suggesting the participation of a late hydrothermal fluid with a more positive $\delta^{34}\text{S}$, potentially from an evaporitic source, as proposed for mineralization in the Marcona/Mina Justa district (Li et al., 2018).

Nickel and Se are redox- and temperature-sensitive elements, and therefore, changes in Ni/Se ratios could be an indicator of changes in temperature, mineral phases, or redox, with potentially more than one factor being important (as discussed previously). The positive correlation of Ni and Se (Fig. 11) may reflect high-temperature conditions, but the high Se and low Ni contents observed in sample LP-1 from group 4 suggest that temperature is not the exclusive control on the concentration of these elements. Changes

in f_{O_2} conditions potentially also played a role in controlling the content of Ni and Se in pyrite. In reduced environments, Se occurs predominantly as Se^{-2} (when Se^{-2} is reduced from Se^0 ; Johnson, 2004), whereas Ni occurs as Ni^{+2} under more oxidizing conditions, above the Ni-NiO redox f_{O_2} buffer (Kress and Carmichael, 1991). Therefore, Ni/Se ratios could potentially be used as a proxy indicative of oxidation states, with higher ratios suggesting more oxidized conditions. Integrating these ratios with $\delta^{34}\text{S}$ data (also redox sensitive) may provide a more robust assessment of redox conditions, where $\delta^{34}\text{S}$ values will tend to be lower at higher f_{O_2} values (Ohmoto, 1972). Nickel/selenium ratios plotted against $\delta^{34}\text{S}$ (Fig. 13) show a rough trend where some of the samples with higher Ni/Se ratios (e.g., LD1493-9, AD357-10, AD357-8) have higher $\delta^{34}\text{S}$ values, and some of the samples with lower Ni/Se ratios (e.g., DH996-2 and LP-1) have lower $\delta^{34}\text{S}$ values. Data from the remaining samples (ES032-5, DH996-21, DH996-23, AD006-26, and ES032-15) do not fall clearly on this trend but can be interpreted as a second potential trend. If these trends are distinct, it is possible that the same process is controlling the correlation between Ni/Se ratios and $\delta^{34}\text{S}$ superimposed on fluids with different background Ni/Se values. Higher Ni/Se ratios and lower $\delta^{34}\text{S}$ values are indicative of a more oxidizing environment; therefore, this general trend may reflect f_{O_2} variation. The presence of mushketovite throughout the district may also relate to changes in the f_{O_2} condition of the hydrothermal fluid (Ohmoto, 2003; Otake et al., 2010). We propose that the formation of mushketovite is related to redox changes, as inferred temperatures for sulfide formation (explained in the next section) are too high for non-redox transformations between Fe oxides ($>250^\circ\text{C}$). Nevertheless, f_{O_2} variation may not be the only factor affecting the

range of $\delta^{34}\text{S}$ values observed in the sample set, as changes in the temperature can also affect $\delta^{34}\text{S}$ isotope values (Ohmoto, 1972). As mentioned above, both Ni and Se are temperature-sensitive elements, while Se has been proposed to be more sensitive to temperature than redox changes (Keith et al., 2017); therefore, varying temperature in addition to f_{O_2} may also explain the poorly defined trends.

Redox variations within a hydrothermal system have been identified as a key process for Cu-Au transport, specifically in porphyry copper systems (Sun et al., 2004, 2013). In magnetite-rich systems, mineralization may be associated with magnetite crystallization, accompanied by decreasing pH and corresponding increase in f_{O_2} . Once sulfate reduction lowers pH sufficiently and the f_{O_2} reaches the hematite-magnetite oxygen fugacity buffer, hematite forms and pH increases for a given f_{O_2} . The oxidation of ferrous iron during the crystallization of magnetite and hematite would be the causal process for sulfate reduction and consequent mineralization (Liang et al., 2009; Jenner et al., 2010; Sun et al., 2013).

In the case of the Candelaria-Punta del Cobre district, deep-seated high-temperature hydrothermal fluids could have channeled upward through structures at sufficient flux rates and fluid/rock ratios to minimize interaction with the host rock, as proposed for the Raúl Condestable deposit (De Haller and Fontboté, 2009). These fluids may have been relatively reduced, hence precipitating the barren early magnetite alteration observed in the district (del Real et al.,

2018). As temperature decreased, hydrothermal fluids would become more oxidized, reaching hematite stability, between 500° and 250°C (Helgeson et al., 1978; Myers and Eugster, 1983; Giggenbach, 1997; Einaudi et al., 2003). As proposed for porphyry deposits, the formation of hematite would increase the pH for a given f_{O_2} causing sulfate reduction and sulfide precipitation (Liang et al., 2009; Jenner et al., 2010; Sun et al., 2013). The replacement of hematite by magnetite (forming muskettovite) implies that conditions became more reduced, possibly as a result of the arrival of multiple pulses of deep-seated hot hydrothermal fluids. Alternative processes, including the influence of local wall rocks or mixing with other fluids, have been suggested as mechanisms for muskettovite formation (De Haller and Fontboté, 2009), but neither clearly explains the concentration of muskettovite in some areas or its overall widespread distribution in all of the deposits in the district.

Temperature and origin of hydrothermal fluids

The $\delta^{34}\text{S}$ values of sulfide-sulfide pairs and sulfide-sulfate pairs that crystallized in equilibrium in hydrothermal systems can be used to estimate the temperature of the hydrothermal fluid at the time of mineralization (Kajiwara and Krouse, 1971; Ohmoto and Lasaga, 1982). Table 4 lists the temperatures calculated using $\delta^{34}\text{S}$ of aqueous sulfide-sulfate (pyrite or chalcopyrite with anhydrite; Ohmoto and Lasaga, 1982) and in situ sulfide-sulfide pairs (pyrite-chalcopyrite in equilibrium;

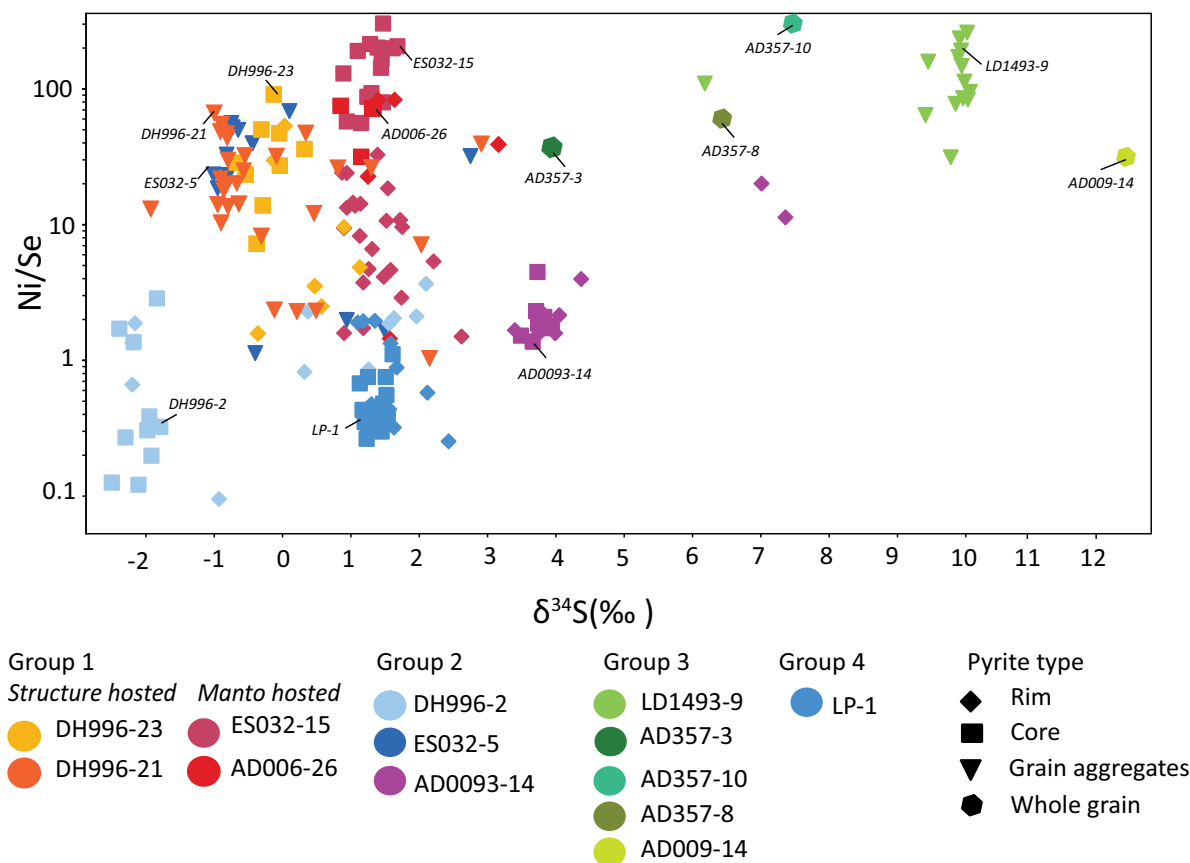


Fig. 13. Pyrite chemistry integrated with $\delta^{34}\text{S}$ measurements; higher Ni/Se ratios roughly correlate with a higher $\delta^{34}\text{S}$. See text for further discussion.

Kajiwaru and Krouse, 1971). The range of temperatures calculated using $\delta^{34}\text{S}$ results of sulfide-sulfate and sulfide-sulfide pairs from the main mineralization event hosted in the lower andesite unit below the manto horizon is 530° to $600 \pm 50^\circ\text{C}$. The range of temperatures calculated using $\delta^{34}\text{S}$ results of sulfide-sulfate and sulfide-sulfide pairs from the dacite dome unit and volcanic-sedimentary unit (both stratigraphically correlated with the manto horizon) varies between 394° and $480 \pm 50^\circ\text{C}$, lower than the temperatures calculated from the stratigraphically deeper samples. Although limited, these results are consistent with cooling of an ascending hydrothermal fluid.

Our results correlate well with previous calculations that estimated that the core of the Fe mineralization in the district formed between 500° and 600°C (Marschik and Fontboté, 2001b) and that Cu-Au mineralization formed from 400° to 500°C (Hopf, 1987). Limited fluid inclusion analyses from quartz and anhydrite in the Candelaria deposit gave homogenization temperatures in the range of 330° to $>470^\circ\text{C}$ (Ulrich and Clark, 1999; Marschik and Chiaradia, 2000), which is consistent with the range of temperatures calculated using sulfide-sulfate and pyrite-chalcocopyrite $\delta^{34}\text{S}$ geothermometry described above. Temperatures calculated for mineralization in the Candelaria-Punta del Cobre district are similar to those calculated for the Mantoverde deposit in Chile and the Marcona/Mina Justa district in Peru using oxygen isotope geothermometry (Chen et al., 2011) and are significantly lower than estimates for IOA deposits and deeper segments of the Candelaria deposit (e.g., 600° – 850°C in Los Colorados, El Romeral, and Cerro Negro Norte in Chile; 400° – 900°C in Kiruna, $>700^\circ\text{C}$ below the Candelaria deposit; Jonsson et al., 2013; Knipping et al., 2015b; Bilenker et al., 2016; Rojas et al., 2018, Salazar et al., 2019; Rodriguez-Mustafá et al., 2020). Temperatures calculated for the manto horizon, where a significant part of the high-grade mineralization is concentrated, partially overlap with the temperatures proposed for mineralization in porphyry copper systems ($\sim 300^\circ$ – 420°C ; Hedenquist and Lowenstern, 1994; Heinrich et al., 2008). Ore deposition is interpreted to occur at $\sim 400^\circ\text{C}$ in porphyry copper environments, with efficient cooling of the hydrothermal fluid being the key to high Cu-Au grades (e.g., Heinrich et al., 2008). A similar interpretation can be suggested for IOCG deposits in the Candelaria-Punta del Cobre district, as the highest grades are associated with temperatures similar to those in porphyry Cu deposits.

The high $\delta^{34}\text{S}$ values ($>10\text{‰}$) obtained for pyrite samples from group 3, as previously mentioned, suggest the addition of an external fluid. Ratios of Se/S can be used as a proxy for tracing hydrothermal fluids in ore systems (e.g., Huston et al., 1995a; Fitzpatrick, 2008; Li et al., 2018), with different fluid sources having distinct Se/S ratios. Seawater (or basinal water ultimately derived from evaporated seawater) has an average $\delta^{34}\text{S}$ value $\sim 21\text{‰}$ and a mass $\Sigma\text{Se}/\Sigma\text{S}$ ratio of ~ 0.0500 to 0.25×10^{-6} , whereas magmatic-hydrothermal fluids have a typical $\delta^{34}\text{S}$ value of ~ 0 with a range of -2 to 2.4‰ for a fluid that exsolved from a crystallizing magma of andesitic composition, and a mass $\Sigma\text{Se}/\Sigma\text{S}$ ratio of ~ 120 to 500×10^{-6} (Huston et al., 1995a; Seal, 2006, and references therein; Fitzpatrick, 2008). When plotting Se/S ratios against $\delta^{34}\text{S}$ isotope values (Fig. 14), the majority of the pyrite samples from group 1 fall within the range of

Table 4. Sulfide-Sulfate and Sulfide-Sulfide Temperatures Calculated Using $\Delta^{34}\text{S}$ Values

Sample	Geothermometer	T ($^\circ\text{C}$)	\pm ($^\circ\text{C}$)	Host rock
AD0357-10	Pyrite-anhydrite	533	50	Lower andesite
AD0357-8	Chalcocopyrite-anhydrite	534	50	Lower andesite
AD0357-3	Pyrite-anhydrite	480	50	Dacite dome
AD009-14	Pyrite-anhydrite	606	50	Lower andesite
AD0093-14	Pyrite-chalcocopyrite	394	50	Dacite dome
DH996-23	Pyrite-chalcocopyrite	552	50	Lower andesite
ES032-15	Pyrite-chalcocopyrite	450	50	Volcanic-sedimentary unit

Notes: Sulfide-sulfate temperatures were calculated using equations by Ohmoto and Lasaga (1982); sulfide-sulfide temperatures were calculated using equations by Kajiwaru and Krouse (1971)

magmatic-hydrothermal fluids (defined by Fitzpatrick, 2008) although showing a spread to lower Se/S ratios. The samples from group 2 show a wider range of values to lower Se/S but at relatively constant $\delta^{34}\text{S}$, although sample AD0093-14 from the dacite dome, together with group 3 samples (in situ and bulk measurements), has higher $\delta^{34}\text{S}$ values and lower Se/S ratios compared with the majority of the pyrite analyses (Fig. 14). Results from these samples are consistent with a different fluid potentially sourced from or equilibrated with basinal rocks. A generalized mixing trend based on previously defined deposition conditions for Se/S (Fitzpatrick, 2008) is suggested on Figure 14 with end-member magmatic-hydrothermal and basin-derived fluids. A similar mixing trend was interpreted for the IOCG mineralization at Mantoverde and Mina Justa IOCG deposits (Benavides et al., 2007; Fitzpatrick, 2008; Li et al., 2018). Additionally, recent $\delta^{18}\text{O}$ data obtained from magnetite samples within the manto horizon in the Candelaria deposit indicate a mixture between magmatic-hydrothermal and external fluids (Rodriguez-Mustafá et al., 2020). The most positive $\delta^{34}\text{S}$ values in the Candelaria-Punta del Cobre district in pyrite from group 3 samples (LD1493-9 and AD009-14) suggest that basin-derived fluids circulated into the Candelaria system toward the end of the main mineralizing event. Further work is needed to test this hypothesis. As all main-phase mineralization samples fall close to, or within, the magmatic-hydrothermal range, it is reasonable to interpret the main ore depositional event as being dominantly of magmatic-hydrothermal origin.

Most of the pyrite analyses in sample DH996-2 plot off the mixing trend, displaying lower Se/S relative to the $\delta^{34}\text{S}$ values. This may reflect lower temperatures, since the fluid-sulfide Se partition coefficient has been proposed to depend on temperature (Fitzpatrick, 2008). As sample DH996-2 comes from the upper part of the Santos deposit, it is possible that system was cooling to lower temperatures in this area.

The Candelaria-Punta del Cobre district has distinct geologic features that may be particularly favorable for IOCG mineralization. The important stratigraphically controlled manto mineralization is hosted by the volcanic-sedimentary unit in the upper part of the Punta del Cobre Formation, below, and locally within, the sedimentary sequence at the base of the Chañarcillo Group. The volcanic-sedimentary unit provided a zone of high permeability that may have been

accessed by deep fluids and also by fluids from the Chañarcillo Group facilitating sulfide precipitation.

Las Pintadas is located at the southern end of the district. Sample LP-1 from Las Pintadas deposit has $\delta^{34}\text{S}$ values and Se/S and Ni/Se ratios that are consistent with the rest of the sample set, suggesting that fluids and processes were generally similar to those in the main part of the district, even though the mineralization is at higher stratigraphic levels than the main cluster of IOCG deposits (Fig. 2). As discussed previously, pyrite in sample LP-1 also has distinct chemical differences from the rest of the sample set, with poor correlations between As and Co and Se and Ni, well-correlated Co and Se, and higher Co and Se contents. The role of different fluids, stratigraphic position, and wall-rock compositions or the distal location of Las Pintadas relative the core of the Candelaria-Punta del Cobre system may have played a role in controlling these differences. Further work would be required to evaluate these options.

Conclusions

Pyrite in samples from IOCG mineralization in several locations and stratigraphic levels within the Candelaria-Punta del Cobre district shows distinct variations of Ni, Co, and Se concentrations that are interpreted to reflect changes in temperature, redox, source of the hydrothermal fluid(s), and potentially stratigraphic/host-rock controls. The $\delta^{34}\text{S}$ isotope values show a range of values (~ -2 to 12‰) where most of the data are concentrated between -2 and 2‰ . The presence of varying Fe oxides (magnetite, partly as mushketovite

and hematite) in the system suggests that changes in the $\delta^{34}\text{S}$ values may correlate with changes in the redox state of the hydrothermal fluid. This may partially explain changes in Ni/Se ratios observed in some of the pyrite samples.

The Co/Ni ratios combined with Se/S and $\delta^{34}\text{S}$ suggest that the fluids responsible for the main mineralization in the district have a magmatic-hydrothermal origin. High $\delta^{34}\text{S}$ values in pyrite from late veins suggest that an externally derived fluid entered the system toward the end of the main mineralizing event. This fluid is interpreted to be of basinal origin, possibly derived from the overlying Chañarcillo Group.

This study demonstrates that pyrite chemistry combined with in situ $\delta^{34}\text{S}$ analyses provides useful information on the fluid sources for IOCG deposits. As outlined, the fluid source and nature of IOCG mineralization has been a topic of debate. Our results concur with recent results from the Mina Justa IOCG deposit in Southern Peru (Li et al., 2018), where mineralization is interpreted to be of magmatic-hydrothermal origin with a late incursion of basin-derived fluids. The results from these deposits do not support formation of IOCG mineralization solely from oxidized saline brines (Barton and Johnson, 1996), at least in the Andean belt.

The Co/Ni ratios and elevated Co and Ni concentrations obtained from the pyrite samples in the district suggest that at least part of the hydrothermal fluid has a mafic igneous affinity, as has been proposed by Chiaradia et al. (2006) on the basis of $\delta^{37}\text{Cl}$ isotope data. Mineralization associated with magmatic fluids of a mafic affinity has been proposed to result from hydrothermal activity driven by mantle underplating

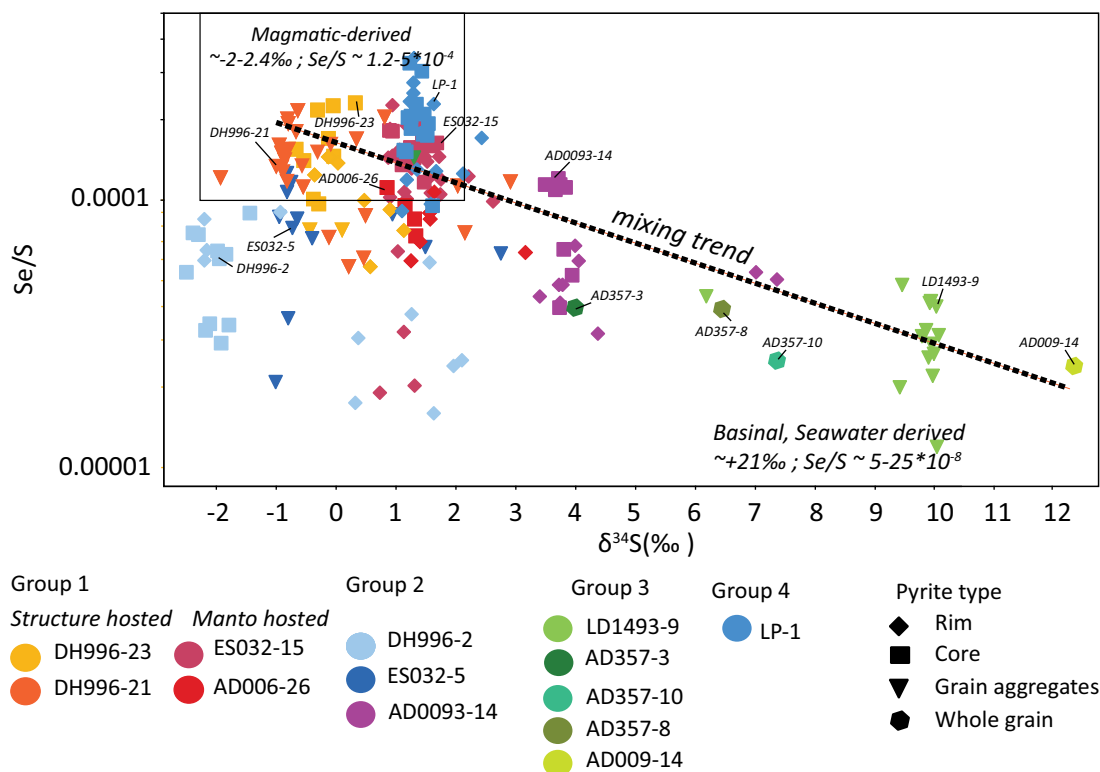


Fig. 14. Pyrite chemistry integrated with $\delta^{34}\text{S}$ measurements on pyrite: Se/S and $\delta^{34}\text{S}$ used for evaluating fluid source; higher $\delta^{34}\text{S}$ and lower Se/S correlate with seawater (or basinal)-derived fluids, lower $\delta^{34}\text{S}$ and higher Se/S correlate with a magmatic-derived fluid. Source ranges were obtained by Fitzpatrick (2008).

(Groves et al., 2010). In the case of the Andean IOCG belt, mineralization is coeval with or immediately follows a long period of subduction-related extension, which could have facilitated back-arc asthenospheric upwelling (Mpodozis and Ramos, 1989). This setting is consistent with a model of mineralization associated with fluids sourced from mafic, probably mantle-derived magmas.

Acknowledgments

Lundin Mining is acknowledged and thanked for funding field support and analytical results. Sulfur isotope analysis were partially funded by National Science Foundation (NSF) grant 1524394 to Adam Simon. Martin Reich thanks support from Millennium Science Initiative through the grant "Millennium Nucleus for Metal Tracing Along Subduction." We thank the support of Louisa Smieska and Rong Huang from the Cornell High Energy Synchrotron source, Jay Thomas and William Nachlas from the Syracuse University EPMA laboratory, Daniel Layton-Matthews and Alexandre Voinot from the Queens Facility for Isotope Research, and finally Kouki Kitajima, John Valley, and Michael Spicuzza from the WiseSIMS laboratory of the University of Madison Wisconsin; WiseSIMS is supported by NSF-EAR1658823 and the University of Wisconsin-Madison. Lluís Fontboté and Lucas Marshall are thanked for thorough reviews that significantly improved the paper.


REFERENCES

- Abratis, P.K., Patrick, R.A.D., and Vaughan, D.J., 2004, Variations in the compositional, textural and electrical properties of natural pyrite: A review. *International Journal of Mineral Processing*, v. 74, p. 41–59.
- Arabasz, W., 1971, Geological and geophysical studies of the Atacama fault zone in northern Chile: Ph.D. thesis, Pasadena, California, California Institute of Technology, 264 p.
- Arévalo, C., 1999, The Coastal Cordillera/Precordillera boundary in the Tierra Amarilla area (27° 20' 27 40'S/70° 05'–70 20'W), northern Chile, and the structural setting of the Candelaria Cu-Au ore deposit: Unpublished Ph.D. thesis, Kingston, Canada, University of Queens.
- Arévalo, C., Grocott, J., Martin, W., Pringle, M., and Taylor, G., 2006, Structural setting of the Candelaria Fe oxide Cu-Au deposit, Chilean Andes (27°30'S): *Economic Geology*, v. 101, p. 819–841.
- Bajwah, Z.U., Seccombe, P.K., and Offler, R., 1987, Trace element distribution, Co:Ni ratios and genesis of the Big Cadia iron-copper deposit, New South Wales, Australia: *Mineralium Deposita*, v. 22, p. 292–300.
- Barker, S.L.L., Hickey, K.A., Cline, J.S., Dipple, G.M., Kilburn, M.R., Vaughan, J.R., and Longo, A.A., 2009, Uncloning invisible gold: Use of nanoSIMS to evaluate gold, trace elements, and sulfur isotopes in pyrite from Carlin-type gold deposits: *Economic Geology*, v. 104, p. 897–904.
- Barra, F., Reich, M., Selby, D., Rojas, P., Simon, A., Salazar, E., and Palma, G., 2017, Unraveling the origin of the Andean IOCG clan: A Re-Os isotope approach: *Ore Geology Reviews*, v. 81, p. 62–78.
- Barton, M.D., and Johnson, D.A., 1996, Evaporitic-source model for igneous-related Fe oxide-(REE-Cu-Au-U) mineralization: *Geology*, v. 24, p. 259–262.
- Benavides, J., Kyser, T.K., Clark, A.H., Oates, C.J., Zamora, R., Tarnovschi, R., and Castillo, B., 2007, The Mantoverde iron oxide-copper-gold district, III Región, Chile: The role of regionally derived, nonmagmatic fluids in chalcopyrite mineralization: *Economic Geology*, v. 102, p. 415–440.
- Bilenker, L.D., Simon, A.C., Reich, M., Lundstrom, C.C., Gajos, N., Bindeman, I., Barra, F., and Munizaga, R., 2016, Fe-O stable isotope pairs elucidate a high-temperature origin of Chilean iron oxide-apatite deposits: *Geochimica et Cosmochimica Acta*, v. 177, p. 94–104.
- Boric, R., Díaz, F., and Maksaev, V., 1990, Geología y yacimientos metaferrosos de la Región de Antofagasta: Servicio Nacional de Geología y Minería, Boletín 40, 246 p.
- Bralia, A., Sabatini, G., and Troja, F., 1979, A reevaluation of the Co/Ni ratio in pyrite as geochemical tool in ore genesis problems: *Mineralium Deposita*, v. 14, p. 353–374.
- Campbell, F.A., and Ethier, V.G., 1984, Nickel and cobalt in pyrrhotite and pyrite from the Faro and Sullivan ore bodies: *The Canadian Mineralogist*, v. 22, p. 503–506.
- Chambers, L.A., 1982, Sulfur isotope study of a modern intertidal environment, and the interpretation of ancient sulfides: *Geochimica et Cosmochimica Acta*, v. 46, p. 721–728.
- Chen, H., Kyser, T.K., and Clark, A.H., 2011, Contrasting fluids and reservoirs in the contiguous Marcona and Mina Justa iron oxide-Cu (-Ag-Au) deposits, south-central Perú: *Mineralium Deposita*, v. 46, p. 677–706.
- Chen, H., Cooke, D.R., and Baker, M.J., 2013, Mesozoic iron oxide copper-gold mineralization in the central Andes and the Gondwana Supercontinent breakup: *Economic Geology*, v. 108, p. 37–44.
- Chiaradia, M., Banks, D., Cliff, R., Marschik, R., and Haller, A., 2006, Origin of fluids in iron oxide-copper-gold deposits: Constraints from ³⁷Cl, ⁸⁷Sr/⁸⁶Sr and Cl/Br: *Mineralium Deposita*, v. 41, p. 565–573.
- Claypool, G.E., Holser, W.T., Kaplan, I.R., Sakai, H., and Zak, I., 1980, The age curves of sulfur and oxygen isotopes in marine sulfate and their mutual interpretation: *Chemical Geology*, v. 28, p. 199–260.
- Cook, N., and Chryssoulis, S.L., 1990, Concentrations of "invisible gold" in the common sulfides: *The Canadian Mineralogist*, v. 28, p. 1–16.
- Cook, N.J., Ciobanu, C.L., and Mao, J., 2009, Textural control on gold distribution in As-free pyrite from the Dongping, Huangtuliang and Hougou gold deposits, North China craton (Hebei Province, China): *Chemical Geology*, v. 264, p. 101–121.
- Corriveau, L., Montreuil, J.F., and Potter, E.G., 2016, Alteration facies linkages among iron oxide copper-gold, iron oxide-apatite, and affiliated deposits in the Great Bear magmatic zone, Northwest Territories, Canada: *Economic Geology*, v. 111, p. 2045–2072.
- Crowe, D.E., and Vaughan, R.G., 1996, Characterization and use of isotopically homogeneous standards for in situ laser microprobe analysis of ³⁴S/³²S ratios: *American Mineralogist*, v. 81, p. 187–193.
- Dale, D., 2015, Praxes software: <https://github.com/praxes/praxes>.
- Deditius, A.P., Utsunomiya, S., Ewing, R.C., Chryssoulis, S.L., Venter, D., and Kesler, S.E., 2009, Decoupled geochemical behavior of As and Cu in hydrothermal systems: *Geology*, v. 37, p. 707–710.
- Deditius, A.P., Kesler, S.E., Ewing, R.C., and Walshe, J., 2011, Trace metal nanoparticles in pyrite: *Ore Geology Reviews*, v. 42, p. 32–46.
- Deditius, A.P., Reich, M., Kesler, S.E., Utsunomiya, S., Chryssoulis, S.L., Walshe, J., and Ewing, R.C., 2014, The coupled geochemistry of Au and As in pyrite from hydrothermal ore deposits: *Geochimica et Cosmochimica Acta*, v. 140, p. 644–670.
- De Haller, A., and Fontboté, L., 2009, The Raul-Condestable iron oxide copper-gold deposit, central coast of Peru: Ore and related hydrothermal alteration, sulfur isotopes, and thermodynamic constraints: *Economic Geology*, v. 104, p. 365–384.
- De Haller, A., Corfu, F., Fontboté, L., Schaltegger, U., Barra, F., Chiaradia, M., Frank, M., and Alvarado, J.Z., 2006, Geology, geochronology, and Hf and Pb isotope data of the Raúl-Condestable iron oxide-copper-gold deposit, central coast of Peru: *Economic Geology*, v. 101, p. 281–310.
- del Real, I., and Arriagada, C., 2015, Inversión tectónica positiva en el distrito El Espino: Relaciones entre deformación, magmatismo y mineralización IOCG, Provincia de Choapa, Chile: XIV Congreso Geológico Chileno, La Serena, 2015, Proceedings, 4 p.
- del Real, I., Thompson, J.F.H., and Carriedo, J., 2018, Lithological and structural controls on the genesis of the Candelaria-Punta del Cobre iron oxide copper gold district, northern Chile: *Ore Geology Reviews*, v. 102, p. 106–153.
- del Real, I., Smieska, L., Thompson, J.F.H., Martínez, C., Thomas, J., and Layton-Matthews, D., 2019, Using multiple micro-analytical techniques for evaluating quantitative synchrotron-XRF elemental mapping of hydrothermal pyrite: *Journal of Analytical and Atomic Spectroscopy*, doi: 10.1039/C9JA00083F.
- Einaudi, M.T., Hedenquist, J.W., and Inan, E.E., 2003, Sulfidation state of fluids in active and extinct hydrothermal systems: Transitions from porphyry to epithermal environments: *Society of Economic Geologists, Special Publication 10*, p. 285–314.
- Espinoza, S., Véliz, H., Esquivel, J., Arias, J., and Moraga, A., 1996, The cupriforous province of the coastal range, northern Chile: *Andean Copper Deposits*, v. 5, p. 19–32.
- Fitzpatrick, A.J., 2008, The measurement of the Se/S ratios in sulphide minerals and their application to ore deposit studies: Ph.D. dissertation, Kingston, Ontario, Canada, Queen's University, 188 p.

- Franchini, M., McFarlane, C., Maydagán, L., Reich, M., Lentz, D.R., Meinert, L., and Bouhier, V., 2015, Trace metals in pyrite and marcasite from the Agua Rica porphyry-high sulfidation epithermal deposit, Catamarca, Argentina: Textural features and metal zoning at the porphyry to epithermal transition: *Ore Geology Reviews*, v. 66, p. 366–387.
- Giggenbach, W.F., 1997, The origin and evolution of fluids in magmatic-hydrothermal systems, in Barnes, H.L., ed., *Geochemistry of hydrothermal ore deposits*, 3rd ed.: New York, Wiley, p. 737–796.
- Gregory, D.D., Large, R.R., Halpin, J.A., Baturina, E.L., Lyons, T.W., Wu, S., Danyushevsky, L., Sack, P.J., Chappaz, A., Maslennikov, V.V., and Bull, S.W., 2015, Trace element content of sedimentary pyrite in black shales: *Economic Geology*, v. 110, p. 1389–1410.
- Griffin, W.L., Ashley, P.M., Ryan, C.G., Sie, S.H., and Suter, G.F., 1991, Pyrite geochemistry in the North Arm epithermal Ag-Au deposit, Queensland, Australia. A proton-microprobe study: *The Canadian Mineralogist*, v. 29, p. 185–198.
- Grocott, J., and Taylor, G.K., 2002, Magmatic arc fault systems, deformation partitioning and emplacement of granitic complexes in the Coastal Cordillera, north Chilean Andes (25 30'S to 27 00'S): *Journal of the Geological Society of London*, v. 159, p. 425–443.
- Grocott, J., Brown, M., Dallmeyer, R.D., Taylor, G.K., and Treloar, P.J., 1994, Mechanisms of continental growth in extensional arcs: An example from the Andean plate-boundary zone: *Geology*, v. 22, p. 391–394.
- Groves, D.I., Bierlein, F.P., Meinert, L.D., and Hitzman, M.W., 2010, Iron oxide copper-gold (IOCG) deposits through earth history: Implications for origin, lithospheric setting, and distinction from other epigenetic iron oxide deposits: *Economic Geology*, v. 105, p. 641–654.
- Gülaçar, O.F., and Delaloye, M., 1976, Geochemistry of nickel, cobalt and copper in alpine-type ultramafic rocks: *Chemical Geology*, v. 17, p. 269–280.
- Hannington, M.D., Poulsen, K.H., Thompson, J.F.H., and Sillitoe, R.H., 1999, Volcanogenic gold in the massive sulfide environment: *Reviews in Economic Geology*, v. 8, p. 325–356.
- Haynes, D.W., Cross, K.C., Bills, R.T., and Reed, M.H., 1995, Olympic Dam ore genesis; a fluid mixing model: *Economic Geology*, v. 90, p. 281–307.
- Hedenquist, J.W., and Lowenstern, J.B., 1994, The role of magmas in the formation of hydrothermal ore deposits: *Nature*, v. 370, p. 519–527.
- Heinrich, C.A., Halter, W., Landtving, M.R., and Pettko, T., 2008, The formation of economic porphyry copper (-gold) deposits: Constraints from microanalysis of fluid and melt inclusions: *Geological Society, London, Special Publications*, v. 248, p. 247–263.
- Helgeson, H.C., Delany, J.M., Nesbitt, H.W., and Bird, D.K., 1978, Summary and critique of the thermodynamic properties of rock-forming minerals: *American Journal of Science*, v. 178, p. 1–229.
- Hitzman, M., 2000, Iron oxide-Cu-Au deposits: What, where, when, and why: Deposits: A global perspective, in Porter, T.M., ed., *Hydrothermal iron oxide copper gold and related deposits: A global perspective*, v. 1: Adelaide, Australian Mineral Foundation, p. 9–25.
- Hitzman, M., Oreskes, N., and Einaudi, M., 1992, Geological characteristics and tectonic setting of proterozoic iron oxide (Cu-U-Au-REE) deposits: *Precambrian Research*, v. 58, p. 241–287.
- Hopf, S., 1987, Petrographische, mineralogische und geochemische Beobachtungen an der Cu-Lagerstätte Agustina/Distrikt Punta del Cobre/Chile: Unpublished Diplomarbeit, Heidelberg, Universität Heidelberg, 144 p.
- Huston, D.L., Sie, S.H., Suter, G.F., Cooke, D.R., and Both, R.A., 1995a, Trace elements in sulfide minerals from eastern Australian volcanic-hosted massive sulfide deposits: Part I. Proton microprobe analyses of pyrite, chalcopyrite, and sphalerite, and Part II. Selenium levels in pyrite; comparison with $\delta^{34}\text{S}$ values and implications for the source of sulfure in volcanogenic hydrothermal systems: *Economic Geology*, v. 90, p. 1167–1196.
- Huston, D.L., Sie, S.H., and Suter, G.F., 1995b, Selenium and its importance to the study of ore genesis: The theoretical basis and its application to volcanic-hosted massive sulfide deposits using PIXE analysis: *Nuclear Instruments and Methods in Physics Research, Section B*, v. 104, p. 476–480.
- Jamtveit, B., 1991, Oscillatory zonation patterns in hydrothermal grossular-andradite garnet: Nonlinear dynamics in regions of immiscibility: *American Mineralogist*, v. 76, p. 1319–1327.
- Jenner, F.E., O'Neill, H.S.C., Arculus, R.J., and Mavrogenes, J.A., 2010, The magnetite crisis in the evolution of arc-related magmas and the initial concentration of Au, Ag and Cu: *Journal of Petrology*, v. 51, p. 2445–2464.
- Johnson, T.M., 2004, A review of mass-dependent fractionation of selenium isotopes and implications for other heavy stable isotopes: *Chemical Geology*, v. 204, p. 201–214.
- Jonsson, E., Troll, V.R., Högdahl, K., Harris, C., Weis, F., Nilsson, K.P., and Skelton, A., 2013, Magmatic origin of giant “Kiruna-type” apatite-iron-oxide ores in central Sweden: *Scientific Reports*, v. 3, article 1644.
- Kajiwar, Y., and Krouse, H.R., 1971, Sulfur isotope partitioning in metallic sulfide systems: *Canadian Journal of Earth Sciences*, v. 8, p. 1397–1408.
- Keith, M., Haase, K.M., Klemm, R., Krumm, S., and Strauss, H., 2016, Systematic variations of trace element and sulfur isotope compositions in pyrite with stratigraphic depth in the Skouriotissa volcanic-hosted massive sulfide deposit, Troodos ophiolite, Cyprus: *Chemical Geology*, v. 423, p. 7–18.
- Keith, M., Smith, D.J., Jenkin, G.R.T., Holwell, D.A., and Dye, M.D., 2017, A review of Te and Se systematics in hydrothermal pyrite from precious metal deposits: Insights into ore-forming processes: *Ore Geology Reviews*, v. 96, p. 269–282.
- Knipping, J.L., Bilenker, L.D., Simon, A.C., Reich, M., Barra, F., Deditius, A.P., Lundstrom, C., Bindeman, I., and Munizaga, R., 2015a, Giant Kiruna-type deposits form by efficient flotation of magmatic magnetite suspensions: *Geology*, v. 43, p. 591–594.
- Knipping, J.L., Bilenker, L.D., Simon, A.C., Reich, M., Barra, F., Deditius, A.P., Wälle, M., Heinrich, C.A., Holtz, F., and Munizaga, R., 2015b, Trace elements in magnetite from massive iron oxide-apatite deposits indicate a combined formation by igneous and magmatic-hydrothermal processes: *Geochimica et Cosmochimica Acta*, v. 171, p. 15–38.
- Koglin, N., Frimmel, H.E., Minter, W.E.L., and Brätz, H., 2010, Trace-element characteristics of different pyrite types in Mesoproterozoic Palaeoproterozoic placer deposits: *Mineralium Deposita*, v. 45, p. 259–280.
- Kozdon, R., Kita, N.T., Huberty, J.M., Fournelle, J.H., Johnson, C.A., and Valley, J.W., 2010, In situ sulfur isotope analysis of sulfide minerals by SIMS: Precision and accuracy, with application to thermometry of ~3.5 Ga Pilbara cherts: *Chemical Geology*, v. 275, p. 243–253.
- Kress, V.C., and Carmichael, I.S.E., 1991, The compressibility of silicate liquids containing Fe_2O_3 and the effect of composition, temperature, oxygen fugacity and pressure on their redox states: *Contributions to Mineralogy and Petrology*, v. 108, p. 82–92.
- Krumm, S., Keith, M., Klemm, R., Strauss, H., and Haase, K.M., 2015, Systematic variations of trace element and sulfur isotope compositions in pyrite with stratigraphic depth in the Skouriotissa volcanic-hosted massive sulfide deposit, Troodos ophiolite, Cyprus: *Chemical Geology*, v. 423, p. 7–18.
- Large, R.R., Danyushevsky, L., Hollit, C., Maslennikov, V., Meffre, S., Gilbert, S., Bull, S., Scott, R., Emsbo, P., Thomas, H., Singh, B., and Foster, J., 2009, Gold and trace element zonation in pyrite using a laser imaging technique: Implications for the timing of gold in orogenic and Carlin-style sediment-hosted deposits: *Economic Geology*, v. 104, p. 635–668.
- Large, R.R., Halpin, J.A., Danyushevsky, L.V., Maslennikov, V.V., Bull, S.W., Long, J.A., Gregory, D.D., Lounejeva, E., Lyons, T.W., Sack, P.J., McGoldrick, P.J., and Calver, C.R., 2014, Trace element content of sedimentary pyrite as a new proxy for deep-time ocean-atmosphere evolution: *Earth and Planetary Science Letters*, v. 389, p. 209–220.
- Lehner, S.W., Savage, K.S., and Ayers, J.C., 2006, Vapor growth and characterization of pyrite (FeS₂) doped with Co, Ni, and As: Variations in semiconducting properties: *Journal of Crystal Growth*, v. 286, p. 306–317.
- Li, R., Chen, H., Xia, X., Yang, Q., Danyushevsky, L.V., and Lai, C., 2018, Using integrated in-situ sulfide trace element geochemistry and sulfur isotopes to trace ore-forming fluids: Example from the Mina Justa IOCG deposit (southern Perú): *Ore Geology Reviews*, v. 101, p. 165–179.
- Liang, H.Y., Sun, W., Su, W.C., and Zartman, R.E., 2009, Porphyry copper-gold mineralization at Yulong, China, promoted by decreasing redox potential during magnetite alteration: *Economic Geology*, v. 104, p. 587–596.
- Longhi, J., Durand, S.R., and Walker, D., 2010, The pattern of Ni and Co abundances in lunar olivines: *Geochimica et Cosmochimica Acta*, v. 74, p. 784–798.
- Lopez, G.P., Hitzman, M.W., and Nelson, E.P., 2014, Alteration patterns and structural controls of the El Espino IOCG mining district, Chile: *Mineralium Deposita*, v. 49, p. 235–259.
- Marschik, R., and Chiaradia, M., 2000, Lead isotope signatures of ore, volcanic, and batholith rocks of the Candelaria-Punta del Cobre area: *International Geological Congress, 31st, Rio de Janeiro, Brazil, August 6–17, 2000, Abstracts, CD-ROM*.
- Marschik, R., and Fontboté, L., 2001a, The Punta del Cobre Formation, Punta del Cobre-Candelaria area, northern Chile: *Journal of South American Earth Sciences*, v. 14, p. 401–433.
- 2001b, The Candelaria-Punta del Cobre iron oxide Cu-Au (-Zn-Ag) deposits, Chile: *Economic Geology*, v. 96, p. 1799–1826.

- Marschik, R., and Söllner, F., 2006, Early Cretaceous U-Pb zircon ages for the Copiapo plutonic complex and implications for the IOCG mineralization at Candelaria, Atacama region, Chile: *Mineralium Deposita*, v. 41, p. 785–801.
- Mathur, R., Marschik, R., Ruiz, J., Munizaga, F., Leveille, R., and Martin, W., 2002, Age of mineralization of the Candelaria Fe oxide Cu-Au deposit and the origin of the Chilean iron belt, based on Re-Os isotopes: *Economic Geology*, v. 97, p. 59–71.
- Monteiro, L., Xavier, R., and Carvalho, E. de, 2008, Spatial and temporal zoning of hydrothermal alteration and mineralization in the Sossego iron oxide-copper-gold deposit, Carajás mineral province, Brazil: *Mineralium Deposita*, v. 43, p. 129–159.
- Mpodozis, C., and Ramos, V.A., 1989, The Andes of Chile and Argentina: Geology of the Andes and its relation to hydrocarbon and mineral resources: Circum-Pacific Council for Energy and Mineral Resources, Earth Science Series, v. 11, p. 59–90.
- Myers, J.T., and Eugster, H.P., 1983, The system Fe-Si-O: Oxygen buffer calibrations to 1,500 K: *Contributions to Mineralogy and Petrology*, v. 82, p. 75–90.
- Nadeau, O., Williams-Jones, A.E., and Stix, J., 2010, Sulphide magma as a source of metals in arc-related magmatic hydrothermal ore fluids: *Nature Geoscience*, v. 3, p. 501–506.
- Nicholls, I.A., Whitford, D.J., Harris, K.L., and Taylor, S.R., 1980, Variation in the geochemistry of mantle sources for tholeiitic and calc-alkaline mafic magmas, Western Sunda volcanic arc, Indonesia: *Chemical Geology*, v. 30, p. 177–199.
- Ohmoto, H., 1972, Systematics of sulfur and carbon isotopes in hydrothermal ore deposits: *Economic Geology*, v. 67, p. 551–578.
- 2003, Nonredox transformations of magnetite-hematite in hydrothermal systems: *Economic Geology*, v. 98, p. 157–161.
- Ohmoto, H., and Goldhaber, M., 1997, Sulfur and carbon isotopes, in Barnes, H.L., ed., *Geochemistry of hydrothermal ore deposits*: Canada, Wiley, p. 517–600.
- Ohmoto, H., and Lasaga, A.C., 1982, Kinetics of reactions between aqueous sulfates and sulfides in hydrothermal systems: *Geochimica et Cosmochimica Acta*, v. 46, p. 6141–6156.
- Otake, T., Wesolowski, D.J., Anovitz, L.M., Allard, L.F., and Ohmoto, H., 2010, Mechanisms of iron oxide transformations in hydrothermal systems: *Geochimica et Cosmochimica Acta*, v. 74, p. 6141–6156.
- Peterson, E., and Mavrogenes, J., 2014, Linking high-grade gold mineralization to earthquake-induced fault-valve processes in the Porgera gold deposit, Papua New Guinea: *Geology*, v. 42, p. 383–386.
- Pollard, P.J., 2006, An intrusion-related origin for Cu-Au mineralization in iron oxide-copper-gold (IOCG) provinces: *Mineralium Deposita*, v. 41, p. 179–187.
- Putnis, A., Fernandez-Diaz, L., and Prieto, M., 1992, Experimentally produced oscillatory zoning in the (Ba, Sr)SO₄ solid solution: *Nature*, v. 358, p. 743–745.
- Reich, M., Kesler, S.E., Utsunomiya, S., Palenik, C.S., Chryssoulis, S.L., and Ewing, R.C., 2005, Solubility of gold in arsenian pyrite: *Geochimica et Cosmochimica Acta*, v. 69, p. 2781–2796.
- Reich, M., Deditius, A., Chryssoulis, S., Li, J.-W., Ma, C.-Q., Parada, M.A., Barra, F., and Mittermayr, F., 2013, Pyrite as a record of hydrothermal fluid evolution in a porphyry copper system: A SIMS/EMPA trace element study: *Geochimica et Cosmochimica Acta*, v. 104, p. 42–62.
- Reich, M., Simon, A., Deditius, A., Barra, F., Chryssoulis, S., et al., 2016, Trace element signature of pyrite from the Los Colorados iron oxide-apatite (IOA) deposit, Chile: A missing link between Andean IOA and iron oxide-copper-gold systems?: *Economic Geology*, v. 111, p. 743–761.
- Requia, K., and Fontboté, L., 1999, Hydrothermal alkali metasomatism in the Salobo iron oxide Cu (-Au) deposit, Carajás mineral province, northern Brazil: *Society for Geology Applied to Mineral Deposits (SGA) Biennial Meeting*, 5th, London, England, August 22–25, 1999, Proceedings, p. 1025–1028.
- Revan, M.K., Genç, Y., Maslennikov, V.V., Maslennikova, S.P., Large, R.R., and Danyushevsky, L.V., 2014, Mineralogy and trace-element geochemistry of sulfide minerals in hydrothermal chimneys from the Upper-Cretaceous VMS deposits of the eastern Pontide orogenic belt (NE Turkey): *Ore Geology Reviews*, v. 63, p. 129–149.
- Richards, J.P., Lopez, G.P., Zhu, J.J., Creaser, R.A., Locock, A.J., and Mumin, A.H., 2017, Contrasting tectonic settings and sulfur contents of magmas associated with Cretaceous porphyry Cu ± Mo ± Au and intrusion-related iron oxide Cu-Au deposits in northern Chile: *Economic Geology*, v. 112, p. 295–318.
- Roberts, D.E., and Hudson, G.R.T., 1983, The Olympic Dam copper-uranium-gold deposit, Roxby Downs, South Australia: *Economic Geology*, v. 78, p. 799–822.
- Rodriguez-Mustafa, M., Simon, A.C., del Real, I., Thompson, J.F.H., Bilenker, L., Barra F., Bindeman I., and David Cadwell, 2020, A continuum from iron oxide copper-gold to iron oxide-apatite deposits: Evidence from Fe and O stable isotopes and trace element chemistry of magnetite: *Economic Geology*, v. 115, p. 1443–1459.
- Rojas, P. A., Barra, F., Reich, M., Deditius, A., Simon, A., Uribe, F., Romero, R., and Rojo, M., 2018, A genetic link between magnetite mineralization and diorite intrusion at the El Romeral iron oxide-apatite deposit, northern Chile: *Mineralium Deposita*, v. 53, p. 947–966.
- Román, N., Reich, M., Leisen, M., Morata, D., Barra, F., and Deditius, A.P., 2019, Geochemical and micro-textural fingerprints of boiling in pyrite: *Geochimica et Cosmochimica Acta*, v. 246, p. 60–85.
- Rudnick, R.L., and Taylor, S.R., 1987, The composition and petrogenesis of the lower crust: A xenolith study: *Journal of Geophysical Research: Solid Earth*, v. 92, p. 13981–14005.
- Rusk, B., Oliver, N., Cleverley, J., Blenkinsop, T., and Zhang, D., 2010, Physical and chemical characteristics of the Ernest Henry iron oxide copper gold deposit, Australia; implications for IOCG genesis, in Porter, T.M., Hydrothermal iron oxide-copper-gold and related deposits: A global perspective: *Advances in the understanding of IOCG deposits*: Linden Park, South Australia, PGC Publishing, Global Perspective Series, v. 3, p. 201–218.
- Rye, R.O., and Ohmoto, H., 1974, Sulfur and carbon isotopes and ore genesis: A review: *Economic Geology*, v. 69, p. 826–842.
- Rye, R.O., Luhr, J.F., and Wasserman, M.D., 1984, Sulfur and oxygen isotopic systematics of the 1982 eruptions of El Chichón volcano, Chiapas, Mexico: *Journal of Volcanology and Geothermal Research*, v. 23, p. 109–123.
- Salazar, E., Barra, F., Reich, M., Simon, A., Leisen, M., Palma, G., Romero, R., and Rojo, M., 2019, Trace element geochemistry of magnetite from the Cerro Negro Norte iron oxide-apatite deposit, northern Chile: *Mineralium Deposita*, v. 55, p. 1–20.
- Seal, R.R., 2006, Sulfur isotope geochemistry of sulfide minerals: *Reviews in Mineralogy and Geochemistry*, v. 61, p. 633–677.
- Sillitoe, R.H., 2003, Iron oxide-copper-gold deposits: An Andean view: *Mineralium Deposita*, v. 38, p. 787–812.
- Simon, A.C., Knipping, J., Reich, M., Barra, F., Deditius, A.P., Bilenker, L., and Childress, T., 2018, Kiruna-type iron oxide-apatite (IOA) and iron oxide-copper-gold (IOCG) deposits form by a combination of igneous and magmatic-hydrothermal processes: Evidence from the Chilean iron belt: *Society of Economic Geologists, Special Publication* 21, p. 89–114.
- Solé, V.A., Papillon, E., Cotte, M., Walter, P., and Susini, J., 2007, A multiplatform code for the analysis of energy-dispersive X-ray fluorescence spectra: *Spectrochimica Acta —Part B Atomic Spectroscopy*, v. 62, p. 63–68.
- Strauss, H., 1997, The isotopic composition of sedimentary sulfur through time: *Palaeogeography Palaeoclimatology Palaeoecology*, v. 132, p. 97–118.
- 1999, Geological evolution from isotope proxy signals—sulfur: *Chemical Geology*, v. 161, p. 89–101.
- Sun, W., Arculus, R.J., Kamenetsky, V.S., and Binns, R.A., 2004, Release of gold-bearing fluids in convergence margin magmas prompted by magnetite crystallization: *Nature*, v. 431, p. 975–978.
- Sun, W., Liang, H., Ling, M., Zhan, M., Ding, X., Zhang, H., Yang, X., Li, Y., Ireland, T.R., Wei, Q., and Fan, W., 2013, The link between reduced porphyry copper deposits and oxidized magmas: *Geochimica et Cosmochimica Acta*, v. 103, p. 263–275.
- Tanner, D., Henley, R.W., Mavrogenes, J.A., and Holden, P., 2016, Sulfur isotope and trace element systematics of zoned pyrite crystals from the El Indio Au-Cu-Ag deposit, Chile: *Contributions to Mineralogy and Petrology*, v. 171, article 33.
- Tardani, D., Reich, M., Deditius, A.P., Chryssoulis, S., Sánchez-Alfaro, P., Wrage, J., and Roberts, M.P., 2017, Copper-arsenic decoupling in an active geothermal system: A link between pyrite and fluid composition: *Geochimica et Cosmochimica Acta*, v. 204, p. 179–204.
- Taylor, S.R., Kaye, M., White, A.J.R., Duncan, A.R., and Ewart, A., 1969, Genetic significance of Co, Cr, Ni, Sc and V content of andesites: *Geochimica et Cosmochimica Acta*, v. 33, p. 275–286.
- Thomson, J., Higgs, N.C., Croudace, I.W., Colley, S., and Hydes, D.J., 1993, Redox zonation of elements at an oxide/post-oxide boundary in deep-sea sediments: *Geochimica et Cosmochimica Acta*, v. 57, p. 579–595.
- Tossell, J.A., Vaughan, D.J., and Burdett, J.K., 1981, Pyrite, marcasite, and arsenopyrite type minerals: Crystal chemical and structural principles: *Physics and Chemistry of Minerals*, v. 7, p. 177–184.

- Ueda, A., and Sakai, H., 1984, Sulfur isotope study of Quaternary volcanic rocks from the Japanese Islands arc: *Geochimica et Cosmochimica Acta*, v. 48, p. 1837–1848.
- Ullrich, T.D., and Clark, A.H., 1999, The Candelaria Cu/Au deposit, III Región, Chile: Paragenesis, geochronology and fluid composition, *in* Stanley, C.J., ed., *Mineral deposits: Processes to processing*: Rotterdam, Balkema, p. 201–204.
- Ushikubo, T., Williford, K.H., Farquhar, J., Johnston, D.T., Van Kranendonk, M.J., and Valley, J.W., 2014, Development of in situ sulfur four-isotope analysis with multiple Faraday cup detectors by SIMS and application to pyrite grains in a Paleoproterozoic glaciogenic sandstone: *Chemical Geology*, v. 383, p. 86–99.
- Williams, P.J., Barton, M.D., Johnson, D.A., Fontboté, L., De Haller, A., Mark, G., Oliver, N.H.S., and Marshick, R., 2005, Iron oxide copper-gold deposits: Geology, space-time distribution, and possible modes of origin: *Economic Geology 100th Anniversary Volume*, p. 371–405.
- Zhao, H.-X., Frimmel, H.E., Jiang, S.-Y., and Dai, B.-Z., 2011, LA-ICP-MS trace element analysis of pyrite from the Xiaolinling gold district, China: Implications for ore genesis: *Ore Geology Reviews*, v. 43, p. 142–153.
- Zhao, X.-F., and Zhou, M.-F., 2011, Fe-Cu deposits in the Kangdian region, SW China: A Proterozoic IOCG (iron-oxide-copper-gold) metallogenic province: *Mineralium Deposita*, v. 46, p. 731–747.



Irene del Real earned her degree in geology from the University of Chile, an M.Sc. degree from the University of British Columbia, Canada, and a Ph.D. degree from Cornell University, USA. Having worked in Cu-Au and Cu-Mo porphyry deposits, and more extensively in iron oxide copper-gold deposits, her research focuses on understanding the genesis and evolution of hydrothermal deposits from a multidisciplinary approach integrating petrological, structural, and geochemical work. Currently she works as a postdoctoral researcher for the Millennium Nucleus Center of Metals Tracing along Subduction at the University of Chile.

